Phase space density analysis of outer radiation belt electron energization and loss during geoeffective and nongeoeffective sheath regions

Kalliokoski, Milla

2022-03

Kalliokoski , M , Kilpua , E , Osmane , A , Jaynes , A N , Turner , D L , George , H , Turc , L & Palmroth , M 2022 , ' Phase space density analysis of outer radiation belt electron energization and loss during geoeffective and nongeoeffective sheath regions ' , Journal of geophysical research. Space physics , vol. 127 , no. 3 , ARTN e2021JA029662 . https://doi.org/10.1029/2021JA029

http://hdl.handle.net/10138/341821
https://doi.org/10.1029/2021JA029662

JGR Space Physics

RESEARCH ARTICLE
10.1029/2021JA029662

Key Points:

- Opposite outer belt response caused by two sheaths: mainly enhancement by geoeffective sheath and depletion by nongeoeffective sheath
- Phase space density analyses of seed, core, and ultrarelativistic electrons reveal importance of ultra-low frequency-driven diffusion and chorus acceleration
- Major variations in wave activity and electron fluxes occur during key sub-regions near the start and end of a sheath

Supporting Information:

Supporting Information may be found in the online version of this article.

Correspondence to:

M. M. H. Kalliokoski,
milla.kalliokoski@helsinki.fi

Citation:

Kalliokoski, M. M. H., Kilpua, E. K. J., Osmane, A., Jaynes, A. N., Turner, D. L., George, H., et al. (2022). Phase space density analysis of outer radiation belt electron energization and loss during geoeffective and nongeoeffective sheath regions. *Journal of Geophysical Research: Space Physics*, *127*, e2021JA029662. https://doi.org/10.1029/2021JA029662

Received 11 JUN 2021
Accepted 29 JAN 2022

Phase Space Density Analysis of Outer Radiation Belt Electron Energization and Loss During Geoeffective and Nongeoeffective Sheath Regions

Milla M. H. Kalliokoski[1], Emilia K. J. Kilpua[1], Adnane Osmane[1], Allison N. Jaynes[2], Drew L. Turner[3], Harriet George[1], Lucile Turc[1], and Minna Palmroth[1,4]

[1]Department of Physics, University of Helsinki, Helsinki, Finland, [2]Department of Physics and Astronomy, University of Iowa, Iowa City, IA, USA, [3]Johns Hopkins University Applied Physics Laboratory, Laurel, MD, USA, [4]Space and Earth Observation Centre, Finnish Meteorological Institute, Helsinki, Finland

Abstract Coronal mass ejection driven sheath regions are one of the key drivers of drastic outer radiation belt responses. The response can however be significantly different based on the sheath properties and the associated inner magnetospheric wave activity. We performed two case studies on the effects of sheaths on outer belt electrons of various energies using data from the Van Allen Probes. One sheath caused a major geomagnetic disturbance and the other had only a minor impact. We especially investigated the phase space density (PSD) of seed, core, and ultrarelativistic electrons to determine the dominant energization and loss processes taking place during the events. Both sheaths produced substantial variation in the electron fluxes from tens of kiloelectronvolts up to ultrarelativistic energies. The responses were however the opposite: the geoeffective sheath mainly led to enhancement, while the nongeoeffective one caused a depletion throughout most of the outer belt. The case studies highlight that both inward and outward radial transport driven by ultra-low frequency waves played an important role in both electron energization and loss. Additionally, PSD radial profiles revealed a local peak that indicated significant acceleration to core energies by chorus waves during the geoeffective event. The distinct responses and different mechanisms in action during these events were related to the timing of the peaked solar wind dynamic pressure causing magnetopause compression, and the differing levels of substorm activity. The most remarkable changes in the radiation belt system occurred in key sheath sub-regions near the shock and the ejecta leading edge.

1. Introduction

The outer Van Allen radiation belt in the Earth's inner magnetosphere hosts electrons over a wide range of energies. These electrons experience significant variations over both short and long timescales driven by various acceleration, transport, and loss processes (e.g., Daglis et al., 2019; Reeves et al., 2016). Adiabatic processes can lead to reversible changes in fluxes (the *Dst* effect, see, e.g., Kim & Chan, 1997) when electrons move radially inward or outward conserving all three adiabatic invariants. Irreversible changes occur when the conservation of one or more adiabatic invariants is violated. Different waves in the inner magnetosphere play a key role in such electron dynamics (see Thorne, 2010). For example, electromagnetic ion cyclotron (EMIC) waves scatter relativistic electrons into the loss cone leading to precipitation loss into the upper atmosphere (e.g., Kurita et al., 2018; Summers & Thorne, 2003). Whistler mode chorus waves can also cause precipitation loss but are rather the dominant cause of local acceleration in the heart of the outer radiation belt (e.g., Bortnik & Thorne, 2007; Jaynes et al., 2015; Thorne et al., 2013). Ultra-low frequency (ULF) wave driven radial transport can act to energize outer belt electrons (e.g., Su et al., 2015) or contribute to losses at the magnetopause (e.g., Shprits et al., 2006; Turner, Shprits, et al., 2012). Understanding which mechanisms govern the outer belt electron dynamics and response under observed solar wind conditions is important for maintaining safe operation of spacecraft traveling through or residing in the belt. This is especially paramount for the increasingly common nanosatellites whose small size limits the amount of shielding making them more vulnerable to anomalies induced by intense electron fluxes.

The key drivers of magnetospheric disturbances are interplanetary coronal mass ejections (ICMEs), stream interaction regions between slow and fast solar wind, and the following high speed streams (e.g., Kilpua, Balogh, von Steiger, & Liu, 2017). Since these large-scale structures generally have different solar wind properties, the response of the outer radiation belt electron populations to them varies (e.g., Kataoka & Miyoshi, 2006; Kilpua et al., 2015; Turner et al., 2019). A typical ICME is composed of a leading shock, a sheath region, and the ejecta.

Similarly, these regions have distinct magnetospheric impact (Kilpua, Koskinen, & Pulkkinen, 2017). Statistical studies of solar wind properties and geomagnetic activity during ICME sheaths indicate that sheaths are associated with elevated interplanetary magnetic field (IMF) magnitude, solar wind speed, density, and dynamic pressure and that their geoeffectiveness depends on the ejecta properties (Kalliokoski et al., 2020; Kilpua et al., 2019; Lugaz et al., 2016; Masías-Meza et al., 2016; Yermolaev et al., 2015, 2017, 2018). Sheaths contain a high level of turbulent fluctuations in the magnetic field (e.g., Moissard et al., 2019). As detailed in previous studies (Hietala et al., 2014; Kalliokoski et al., 2020; Kilpua et al., 2013, 2015), sheaths tend to cause intense wave activity in the inner magnetosphere, in particular EMIC and ULF Pc5 waves, as well as strong compression of the magnetosphere. The response of electron populations in the outer radiation belt can also be different during sheaths and ejecta. In particular, the turbulent and compressed sheaths can cause deep and sustained depletion of MeV electrons (Alves et al., 2016; Da Silva et al., 2020; Hietala et al., 2014; Kalliokoski et al., 2020; Kilpua et al., 2015), but can also lead to their enhancement (Turner et al., 2019). Turner et al. (2019) also found that sheaths tend to cause a two-part outer belt structure at MeV energies.

Many studies of the outer radiation belt response consider events generating moderate or stronger geomagnetic storms (e.g., evaluated with *Dst* or *SYM-H* index dropping below −50 nT; Gonzalez et al., 1994) and assess the changes in electron flux over long time periods, up to a few days, and can even exclude the day of the storm in their quantitative analysis (e.g., Moya et al., 2017; O'Brien et al., 2001; Reeves et al., 2003; Turner et al., 2015). Investigations of the response to sheaths have generally used a similar approach (Kilpua et al., 2015; Turner et al., 2019). It has however been shown that significant variation in the outer belt electron fluxes can occur also during small storms and nonstorm periods (e.g., Anderson et al., 2015; Katsavrias et al., 2015; Schiller et al., 2014). The statistical analysis in Kalliokoski et al. (2020) detailed the immediate (6 hr) response of the outer belt electrons to both geoeffective and nongeoeffective sheaths from source to ultrarelativistic energies (10s keV to several MeV). Regardless of whether they cause a geomagnetic storm or not, sheaths predominantly deplete the outer parts ($L > 4$) of the outer belt at core and ultrarelativistic energies. Geoeffective sheaths often cause depletion also at lower L-shells at MeV energies. Source and seed electron populations (10s–100s keV) are similarly enhanced at $L > 4$ during sheaths, while the geoeffective sheaths also enhance the fluxes at $L < 4$. The study also revealed a clear energy dependence of the depletion. While losses mainly occur at MeV energies, the likelihood of depletion of the seed population (100s keV) increases with radial distance. This was concluded to be likely due to wave-particle interactions dominating the losses in the inner part of the belt, in particular by EMIC waves that can cause rapid loss at MeV energies (e.g., Kurita et al., 2018; Summers & Thorne, 2003), and due to intense substorms effectively replenishing the source and seed populations. Losses at high L-shells were suggested to be dominated by magnetopause shadowing arising from the combination of the magnetopause inward incursion and ULF Pc5 wave driven outward radial transport (e.g., Turner, Shprits, et al., 2012). The determination of the exact physical mechanisms causing the depletion and enhancement during sheaths however needs a more detailed analysis.

Phase space density (PSD), which is obtained by dividing electron fluxes by momentum squared, combined with the conversion from a function of energy and pitch angle into adiabatic invariant coordinates (see, e.g., Green & Kivelson, 2004), provides a useful tool for such analysis. Since the PSD remains constant for adiabatic processes, the evolution of the shape of PSD radial profiles can be used to infer the electron acceleration and loss mechanisms in the radiation belts (e.g., Chen, Reeves, & Friedel, 2007; Green, 2006; Shprits et al., 2017; Turner, Shprits, et al., 2012). That is, PSD allows for distinguishing between adiabatic and nonadiabatic effects, as well as between local acceleration and local losses from those caused by inward or outward radial transport or diffusion and magnetopause shadowing. A drawback of the method is that calculating the adiabatic invariants requires the use of a global geomagnetic field model. Deviations in the model from the real conditions, especially during storms when the magnetosphere becomes complex, lead to uncertainties in PSD (Boyd et al., 2014; Chen, Friedel, et al., 2007; Morley et al., 2013). Uncertainties are also introduced by errors in the instrument measurements and possible interpolations and fits that need to be done to acquire adequate resolution in PSD (Turner, Angelopoulos, et al., 2012). Nevertheless, careful PSD analysis is advantageous in investigating nonadiabatic outer belt electron dynamics on short timescales, for example, during the sheath and ejecta of an ICME (Da Silva et al., 2020).

Da Silva et al. (2020) studied an ICME sheath region that produced a small geomagnetic storm and a dropout in relativistic electron fluxes. Examining wave measurements and modeling results, they found that the dropout was

likely caused by magnetopause shadowing along with ULF wave driven outward radial diffusion and local loss via pitch angle scattering by chorus and EMIC waves, which was confirmed by the PSD analysis. They concluded that wave-particle interactions were efficient only during the sheath, and thus different ICME sub-structures generate a different outer belt response. It is therefore interesting to compare whether similar processes dominate the electron response during other sheaths. In fact, our study highlights the importance of radial diffusion by ULF waves combined with losses at the magnetopause, and the magnitude of this loss is related to the duration of the magnetopause compression. One of our ICME sheath events also caused significant energization by local chorus acceleration, where the presence of chorus waves was inferred from the precipitation loss they caused at lower energies.

In this article, we analyze the outer radiation belt electron response to two distinct ICME sheaths. One sheath was geoeffective causing a notable magnetospheric disturbance (min. *SYM-H* of −90 nT), while the other was nongeoeffective, that is, it did not cause a significant geomagnetic storm (min. *SYM-H* of −32 nT). This selection of events allows us to compare how the outer belt electron populations are shaped by a geoeffective and a nongeoeffective sheath, both of which can be important for radiation belt electron dynamics but which have significant differences in their responses, as indicated by Kalliokoski et al. (2020). Similar to earlier studies (e.g., Hietala et al., 2014; Kalliokoski et al., 2020; Kilpua et al., 2019, 2015), this work highlights that significant variations occur in the outer belt electron fluxes during ICME-driven sheath regions. We further show that such drastic changes can also arise at ultrarelativistic energies (>3 MeV), and even during a nongeoeffective sheath. Such relatively short timescale variations (<∼12 hr) are missed by studies considering the electron response over the whole geomagnetic storm period that often lasts for several days. In contrast to the prior sheath studies, we perform a detailed analysis of electron PSD which, combined with consideration of the inner magnetospheric wave activity, sheds light on the dominant mechanisms that act on the outer belt electrons. We focus on the nonadiabatic dynamics driven specifically by the sheath region impact, and our aim is to compare and contrast how the outer radiation belt responds to sheaths with different properties. This reveals the opposite overall response between the geoeffective and nongeoeffective sheaths: the former enhancing most of the electron populations and the latter depleting most of the outer belt.

The various data and methodology used in this study are presented in Section 2. In Section 3, we describe the observations of the properties of the two sheaths, as well as the activity of waves and the outer belt conditions in terms of both electron flux and PSD during the sheath events. We discuss the results and especially the interpretation of the PSD radial profiles in Section 4 and conclude in Section 5.

2. Data and Methodology

2.1. Solar Wind Data

We considered two ICMEs with sheath regions, the first arriving on 2 October 2013 and the other on 15 February 2014. The timing of the sheath regions were based on the shock times from the University of Helsinki Heliospheric Shock Database (http://www.ipshocks.fi, last access: 4 June 2021) and visual inspection of the solar wind data to determine the ejecta interval. The characteristics of sheath regions and ejecta and the determination of their boundaries are discussed, for example, in Richardson and Cane (2010) and Kilpua, Koskinen, and Pulkkinen (2017). Both events are listed as magnetic clouds in the Richardson and Cane ICME list (http://www.srl.caltech.edu/ACE/ASC/DATA/level3/icmetable2.htm, last access: 4 June 2021), that is, the ejecta have signatures of a magnetic flux rope.

We used solar wind data measured by the Wind spacecraft at 1 min resolution (Lepping et al., 1995; Ogilvie et al., 1995). We propagated the Wind data to the bow shock nose. We estimated the propagation time by dividing the distance between $L1$ point and the bow shock nose by the mean solar wind speed during the considered interval. The bow shock nose distance and geomagnetic activity indices (*AL* and *SYM-H*) were acquired from the OMNI database at 1 min resolution. Both Wind and OMNI data were obtained via the NASA Goddard Space Flight Center Coordinated Data Analysis Web (CDAWeb, https://cdaweb.gsfc.nasa.gov/index.html/, last access: 4 June 2021). We used the Wind data instead of solar wind properties from OMNI database since the latter had data gaps during the periods of interest. The solar wind data were also used to calculate the subsolar magnetopause location with the Shue et al. (1998) model.

2.2. Wave Activity

The ULF Pc5 pulsations and electromagnetic ion cyclotron (EMIC) waves were obtained from a Geostationary Operational Environmental Satellite (GOES) at $L \sim 6.6$. The magnetic field data have a time resolution of 0.512 s (Singer et al., 1996). We derived the ULF power spectrum via wavelet analysis of the magnetic field magnitude measured by GOES-13 and GOES-15, and calculated the mean over the frequency range 2–7 mHz for Pc5 pulsations and 0.1–1 Hz for EMIC waves (Jacobs et al., 1964), where the upper bound for EMIC waves is restricted by the GOES time resolution. GOES measurements are subject to diurnal variations due to local time dependency of the field strength. Measurements of ULF Pc5 and EMIC wave activity at the geostationary orbit do not necessarily always reflect the wave activity elsewhere in the radiation belts (Engebretson et al., 2018; Georgiou et al., 2018).

For this reason, we calculated ULF Pc5 wave power with the same technique from the magnetic field magnitude measured by the Electric and Magnetic Field Instrument Suite and Integrated Science (EMFISIS; Kletzing et al., 2013) on the Van Allen Probes. We used the 1 s averaged level-3 data available on the EMFISIS webpage (https://emfisis.physics.uiowa.edu/data/index, last access: 4 June 2021). This allows us to confirm the ULF wave activity in the heart of the outer radiation belt, which may not always be represented by observations at geostationary orbit (Engebretson et al., 2018; Georgiou et al., 2018). The magnetic field magnitude increases rapidly when the Van Allen Probes approach the Earth at perigee of their orbits, causing the ULF wave power to spike. We have thus ignored times at perigee based on the radial location of the spacecraft. We obtained the positional information from the Van Allen Probes ephemeris data (available from https://rbsp-ect.newmexicoconsortium.org, last access: 4 June 2021).

Data of very low frequency (VLF) wave activity, namely whistler mode chorus and plasmaspheric hiss, were also obtained from EMFISIS on the Van Allen Probes. Specifically, we used the level-2 waveform receiver diagonal spectral matrix data that have a frequency range from 2 Hz to 12 kHz and 6 s time cadence. Lower band chorus has the frequency range 0.1–0.5 f_{ce} and upper band chorus has 0.5–0.8 f_{ce} (Burtis & Helliwell, 1969; Koons & Roeder, 1990), where f_{ce} is the electron cyclotron frequency, which was here obtained from the Tsyganenko and Sitnov (2005) geomagnetic field model (TS04D). Chorus waves occur outside the dense plasmasphere, whereas plasmaspheric hiss occurs inside the plasmasphere at frequencies from 100 Hz to 0.1 f_{ce}. To discriminate chorus from plasmaspheric hiss, we used electron density of 100 cm^{-3} as an estimation of the plasmapause location (e.g., Malaspina et al., 2018). The electron density is provided as a level-4 data product by the EMFISIS team and is derived from the upper hybrid resonance frequency (Kurth et al., 2015).

Van Allen Probes measure the local chorus wave activity and can therefore miss the global chorus distribution. This is especially the case when the perigee of the spacecraft is in the dawn sector (i.e., when spacecraft are at $L < 4$ on the dawnside) because chorus predominantly occurs at $L > 4$ on the dawnside (e.g., Lam et al., 2010). In both considered events, little local chorus activity was observed by Van Allen Probes. The perigee of both spacecraft was at dawn for the 2 October 2013 event and at midnight for the 15 February 2014 event, indicating that their observations might not reflect the global chorus activity. Thus, we used low-energy electron precipitation data as a proxy for chorus activity (Chen et al., 2014).

Electron precipitation data is provided by the low-altitude and polar-orbiting Polar Operational Environmental Satellites (POES). We used data from the Medium Energy Proton and Electron Detector (MEPED) instrument of the Space Environment Monitor (SEM-2; Evans & Greer, 2004) suite on board six such polar-orbiting spacecraft (NOAA-15, NOAA-16, NOAA-18, NOAA-19, MetOp-A, and MetOp-B). MEPED measures electrons with the 0° and 90° telescopes at energies >30, >100, and >300 keV. The MEPED data used here has been reprocessed (Asikainen, 2017; Asikainen & Mursula, 2013) to correct for proton contamination and other instrumental problems that affect the POES measurements (see, e.g., Rodger et al., 2013).

While the MEPED 0° and 90° telescopes are intended to measure the precipitating and trapped fluxes, respectively, they collect electrons from a combination of radiation belt populations. At high latitudes, which were considered in this study, the 0° telescope underestimates precipitating fluxes as the bounce loss cone is significantly larger than the field of view of the detector (Rodger et al., 2013). On the other hand, at high latitudes, the 90° telescope measures fluxes in the bounce and drift loss cones, possibly not measuring the trapped fluxes at all (Rodger et al., 2010). To estimate the low-energy electron precipitation, we combined the data from the two

telescopes and considered the geometric mean of the fluxes (e.g., George et al., 2020; Hargreaves et al., 2010; Rodger et al., 2013):

$$j_{precip} = \sqrt{j_0 * j_{90}}, \quad (1)$$

where j_0 and j_{90} are the fluxes from the 0° and 90° telescopes, respectively. Since we are considering precipitation qualitatively, we expect this method to provide a better estimate of the precipitating fluxes than the 0° telescope measurements alone.

We used the chorus proxy derived by Chen et al. (2014) which gives the chorus wave power as

$$B_w^2(L) = \frac{j_{precip}(L)}{P * \left[(L-3)^2 + 0.03\right]}, \quad (2)$$

where P is a scaling factor. The proxy is restricted to $L > 3.5$. The Van Allen Probes detected almost no chorus waves, so we did not scale the proxy with spacecraft chorus observations and set $P = 1$, which suffices for our qualitative analysis of the chorus activity.

Following Chen et al. (2014), we calculated the chorus proxy for low-energy (30–100 keV) electrons. That is, we subtracted the POES > 100 keV electron channel measurements from the >30 keV measurements for each detector and combined the data using Equation 1. The data was then binned 0.1 in L-shell and 100 min in time, which corresponds to the orbital period of POES spacecraft. The high resolution data from multiple spacecraft on polar orbits allow us to inspect the chorus proxy up to high L-shells, and here we show the proxy up to $L = 10$. While all magnetic local times (MLT) are included in the chorus proxy used in the final analysis, we additionally analyzed the proxy in limited MLT ranges. This local chorus proxy had peak activity on the dawnside, which is the expected location of peak chorus activity. This indicates that the Chen et al. (2014) proxy is dominated by chorus.

2.3. Electron Flux Data and Outer Belt Response Parameter

Outer radiation belt electron fluxes were obtained from the Energetic Particle, Composition, and Thermal Plasma instrument suite (ECT; Spence et al., 2013) on board the twin Van Allen Probes, which provide a wide coverage in electron energy at radial distances up to $L = 6$ (Mauk et al., 2013). The Magnetic Electron Ion Spectrometer (MagEIS; Blake et al., 2013) observes the source, seed and core electron populations from 30 keV to 1.5 MeV, while the Relativistic Electron Proton Telescope (REPT; Baker, Kanekal, Hoxie, Batiste, et al., 2013) measures the core and ultrarelativistic populations from 1.8 to 10 MeV. These data are available on the ECT website (https://rbsp-ect.newmexicoconsortium.org, last access: 4 June 2021). We used the level-2 spin-averaged differential electron fluxes for response parameter calculation and the level-3 pitch angle resolved fluxes for computing PSD. The employed MagEIS fluxes are background corrected (Claudepierre et al., 2015), as available in the MagEIS data product, unless stated otherwise. We have only used MagEIS data with less than 75% errors (e.g., Boyd et al., 2019). The L-shell information of the spacecraft, derived from the Tsyganenko and Sitnov (2005) geomagnetic field model, were acquired from the magnetic ephemeris data that are also available on the ECT website.

We determined the outer radiation belt electron response to the sheath region, following Kalliokoski et al. (2020), by calculating the response parameter (R) as the ratio of the post-sheath flux average to the pre-sheath flux average. The flux average was taken over 6 hr, which allowed for a sufficient L-shell coverage. The response parameter was computed for 0.1 sized L-shell bins in $L = 2$–6 using electron flux data from both Van Allen Probes. We calculated the response parameter for four energy channels representing the source (54 keV), seed (346 keV), core (1575 keV), and ultrarelativistic (4.2 MeV) populations. The electron response is characterized as *depletion* when the flux average decreased by over a factor of 2 ($R < 0.5$) and *enhancement* when the flux average increased by over a factor of 2 ($R > 2$).

The method of computing the response parameter is adapted from Reeves et al. (2003) and Turner et al. (2015, 2019), who applied it to study the outer belt response to entire geomagnetic storms and considered periods ranging from 12 hr up to a few days. In contrast, we focus here on the net effect of changes in electron fluxes due to the sheath region that are observed immediately after the sheath, which we aim to capture with the 6 hr averaging period.

The post-sheath flux average is embedded in the ejecta, but we expect the main response due to the ejecta to occur at later times. We do note that the ejecta in both studied events were shorter than the sheath regions. The ejecta duration is 15.0 hr on the 2 October 2013 event and 8.6 hr on the 15 February 2014 event—the latter is close to the averaging period but we see that the main changes in electron fluxes occurred during the sheath region. The ejecta times match approximately with those reported in the Richardson and Cane ICME list.

2.4. PSD Analysis

For a more detailed investigation of the acceleration, transport, and loss processes taking place during the events, we calculated the PSD at chosen adiabatic invariant coordinates (e.g., Chen et al., 2005; Chen, Reeves, & Friedel, 2007; Green, 2006; Green & Kivelson, 2001, 2004; Shprits et al., 2017; Turner, Angelopoulos, Li, et al., 2014; Turner, Shprits, et al., 2012). Adiabatic invariants correspond to the three constants of motion in the geomagnetic field when changes occur slowly (e.g., Roederer, 1970): gyration about field lines (first invariant, μ), bounce along field lines (second invariant, K), and drift about the Earth (third invariant, L^*). L^* illustrates the radial distance of magnetic field lines in a nondipolar field (more strictly, L^* is the equatorial radial distance where a particle on a given field line would be found if all nondipolar perturbations were adiabatically turned off; see Roederer, 1970). It is pertinent to use the L^* parameter to interpret PSD, while L-shell is more suitable for other variables, here electron fluxes and chorus proxy. The difference in L and L^* is largest at apogee with L^* being ∼0.5–1 units lower than L. The differences of these parameters do not affect our qualitative comparisons of PSD and other variables.

We used pitch angle resolved electron fluxes from MagEIS and REPT on both Van Allen Probes to compute PSD. The size of the pitch angle bins is 16.4° for MagEIS and 10.6° for REPT. We acquired invariants K and L^* from the ECT magnetic ephemeris files that are computed with the global magnetic field model of Tsyganenko and Sitnov (2005; TS04D; https://rbsp-ect.newmexicoconsortium.org, last access: 4 June 2021). The time resolution of these modeled parameters is typically 5 min and the pitch angle resolution is 5°. K and L^* were interpolated to the equatorial pitch angles, which were mapped from the Van Allen Probes local pitch angle measurements using the TS04D modeled equatorial magnetic field magnitude. The magnetic moment μ was calculated using the magnetic field magnitude observed by Van Allen Probes magnetometers (EMFISIS; Kletzing et al., 2013) and the local pitch angle measurements. The electron fluxes were binned to 1 min prior to calculating PSD.

We used all low and medium energy channels from MagEIS, except the highest medium channel that was replaced by the first MagEIS high channel. The employed MagEIS channels cover the energy range from 30 keV to 1 MeV, while we used REPT to capture the high energy electrons from 1.8 to 9.9 MeV. In order to improve the energy resolution for the PSD calculation, we added two artificial energy channels in between each instrumental channel. Fluxes in these added channels were linearly interpolated in log-log (flux-energy) space from the measured fluxes in the two neighboring instrumental channels. We performed this interpolation between the two instrumental channels only if both had a measurement available (i.e., if either had a fill value in the given time and pitch angle bin, we set the flux in the artificial channels to a fill value). The central energies of the artificial channels were defined as the geometric mean of the lower and upper limits as defined in Chen et al. (2005). We also followed the Chen et al. (2005) formulation in calculating the relativistic momenta for each channel and converting electron fluxes to PSD. The steps in the calculation of PSD at fixed μ and K are summarized in, for example, Hartley and Denton (2014). We note that no fitting of the energy or pitch angle distributions were performed in our method.

We investigated electrons mirroring near the equator by fixing K to an upper limit of 0.05 $R_E G^{1/2}$. We focus on two energy ranges, $\mu = (300 \pm 10)$ MeV/G and $\mu = (3{,}000 \pm 100)$ MeV/G, where the PSD was calculated using MagEIS and REPT data, respectively. We note that the electron energy corresponding to the chosen μ value depends on L^*, decreasing toward higher L^*. The energy corresponding to $\mu = (300 \pm 10)$ MeV/G ranges from about 300 keV at $L^* \sim 5$ to 1 MeV at $L^* \sim 3$. It thus samples both the seed and core populations. The other value, $\mu = (3{,}000 \pm 100)$ MeV/G, samples the core population above $L^* \sim 4$ and the ultrarelativistic population at lower L^*. The energy ranges from about 2 to 5 MeV at $L^* = 3$–5. The energy as a function of L^* is presented in the Supporting Information (Figure S3), where we have also shown the pitch angles corresponding to the chosen K range as a function of L^* (Figure S4). We note that the pitch angles are most of the time above ∼70°, but Van Allen Probe A also samples electrons with ∼40° pitch angle at $L^* = 4.5$–5.5.

The PSD values were binned to $\Delta L^* = 0.15$ when plotting the PSD profiles as a function of L^*, as multiple values of PSD can be found at similar L^*. The purpose of the binning is to smooth the profiles and indicate the average shape of the curves. We have provided the unbinned PSD profiles in the Supporting Information (Figure S5).

The fluctuations in PSD at similar L^* arises from the employed ranges in μ and K. These ranges are broad enough for PSD points with μ and K values within these ranges to be found at two or more energy channels or pitch angle bins at the same time. The different bins correspond to different values of PSD, but have similar L^*, causing the fluctuations. Fluctuations seem to arise in particular from large jumps (approximate order of magnitude) in flux between REPT energy channels. Similar fluctuation effects are seen in other PSD studies using μ and K ranges (e.g., Schiller et al., 2014). Naturally, the fluctuations increase for larger ranges of μ and K. The additional interpolated energy channels, while increasing the energy resolution, reproduce the fluctuations originating from flux variation between the instrumental channels. On the other hand, these ranges allow for a better resolution in PSD as opposed to fixing μ and K to a single value. We have chosen the ranges for this study as a compromise of being restrictive enough to remove major fluctuations, but broad enough to allow for a sufficient resolution of PSD points as a function of L^*.

3. Results

In this section, we present the geospace response following the two ICME events with sheath regions occurring on 2 October 2013 and 15 February 2014, in terms of solar wind parameters, geomagnetic activity indices, inner magnetospheric wave activity, outer radiation belt electron fluxes, and PSD.

3.1. Overview of Solar Wind Observations

Figure 1 shows the evolution of solar wind parameters and geomagnetic activity during the two analyzed events, 2 October 2013 (Event 1) on the left and 15 February 2014 (Event 2) on the right. The panels present the magnetic field magnitude, magnetic field components in Geocentric Solar Magnetospheric (GSM) coordinate system, solar wind speed, solar wind dynamic pressure, and subsolar magnetopause position from the Shue et al. (1998) model, and *AL* and *SYM-H* indices. The sheath is depicted with the blue shaded area.

For Event 1, the shock associated with the sheath region was observed by Wind on 2 October 2013 at 1:11 UT (or at 1:58 UT when time-shifted to the magnetopause). The sheath extended until 23:50 UT on the same day (0:37 UT on the next day at magnetopause), spanning 22.7 hr. The IMF components exhibited large-amplitude fluctuations. The IMF magnitude and solar wind dynamic pressure were enhanced during the front part of the sheath region, which was concurrent with the largest geomagnetic impact, as shown by both the *SYM-H* and *AL* indices. The sheath caused a moderate geomagnetic storm with a minimum *SYM-H* of −90 nT reached shortly after the shock impact. The IMF *Bz*-component changed from strongly negative to positive after a few hours in the sheath and turned slightly negative near the end of the sheath causing some substorm activity. The ejecta did not cause a geomagnetic storm or any substorm activity as the *Bz*-component was positive during the ejecta. The subsolar magnetopause was compressed beyond 10 Earth radii and briefly beyond the geostationary orbit during the front part of the sheath region. After reaching the minimum value, the magnetopause gradually relaxed to a nominal position during the rest of the sheath and moved to large distances (∼15 R_E) during the low dynamic pressure ejecta.

The shock of Event 2 was observed on 15 February 2014 at 12:46 UT (13:47 UT at magnetopause) and the sheath lasted until 16 February at 4:00 UT (5:01 UT at magnetopause), that is, the sheath duration was 15.2 hr. The IMF components presented again large-amplitude fluctuations during the sheath, but now the largest fluctuations with southward fields occurred in the trailing part of the sheath. In the front part of the sheath, the IMF was directed northward. Dynamic pressure was elevated and peaked at the center of the sheath, and consequently, the magnetopause reached closest to Earth in the middle of the sheath. Again, the magnetopause was briefly pushed beyond geostationary orbit. The magnetopause then relaxed back to its nominal position during the ejecta. There was some substorm activity during the sheath, as evidenced by the *AL* index. A small substorm occurred just after the shock passage, while a bigger took place close to the sheath trailing edge. The *SYM-H* index was first positive during most of the sheath and then decreased to minimum value of −32 nT at the very end of the sheath. The *SYM-H* index remained negative but above −30 nT during the ejecta.

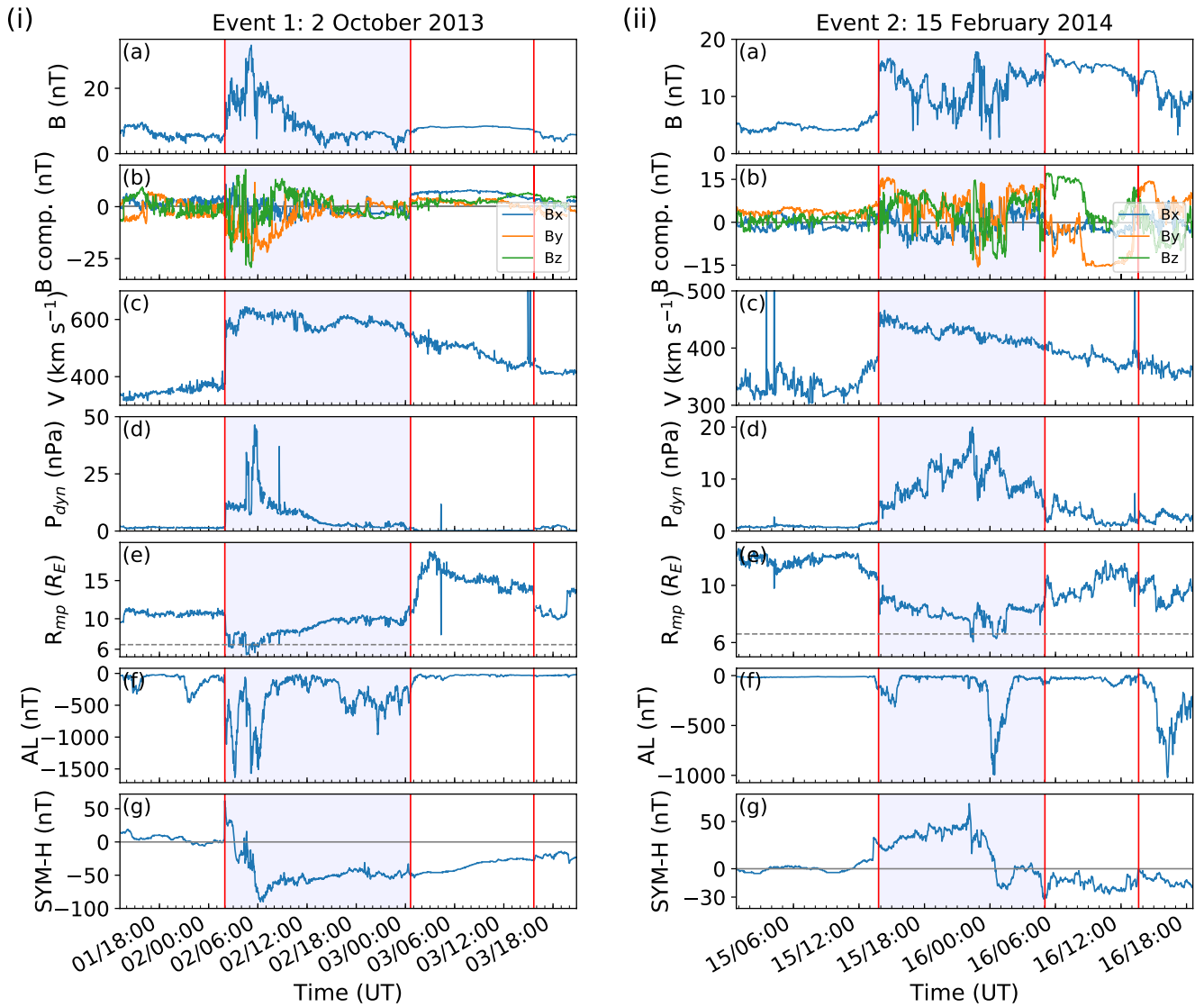

Figure 1. Solar wind properties and geomagnetic activity indices for the sheath events (i) on 2 October 2013 and (ii) on 15 February 2014. (a) Magnetic field magnitude, (b) magnetic field components in the geocentric solar magnetospheric coordinate system, (c) solar wind speed, (d) solar wind dynamic pressure, (e) subsolar magnetopause location from the Shue et al. (1998) model with the location of the geostationary orbit indicated (6.6 R_E), (f) *AL* index, and (g) *SYM-H* index. The red vertical lines indicate the shock, ICME ejecta leading edge, and ejecta trailing edge in UT (universal time). The shaded area marks the sheath interval. The Wind data has been shifted from *L*1 to the magnetopause.

The main difference between the two events was the intensity of the geomagnetic storm, as evidenced by the *SYM-H* index, and the timing of the strong substorm activity, seen in the *AL* index, which coincided with the *SYM-H* minimum. Stronger geomagnetic activity occurred near the start of the sheath with a −90 nT *SYM-H* minimum for the geoeffective Event 1. On the contrary, for the nongeoeffective Event 2, which had a *SYM-H* minimum of −32 nT, the stronger substorm activity occurred near the end of the sheath.

3.2. Inner Magnetospheric Wave Activity

The wave activity in the inner magnetosphere is shown in Figure 2. Again the left panels show the data for Event 1 and the right panels for Event 2. The top panels show the ULF Pc5 wave power from Van Allen Probe A, and the bottom panels show the ULF Pc5 and EMIC wave powers from GOES-15. A similar plot for Van Allen Probe B and GOES-13 is found in the Supporting Information (Figure S1).

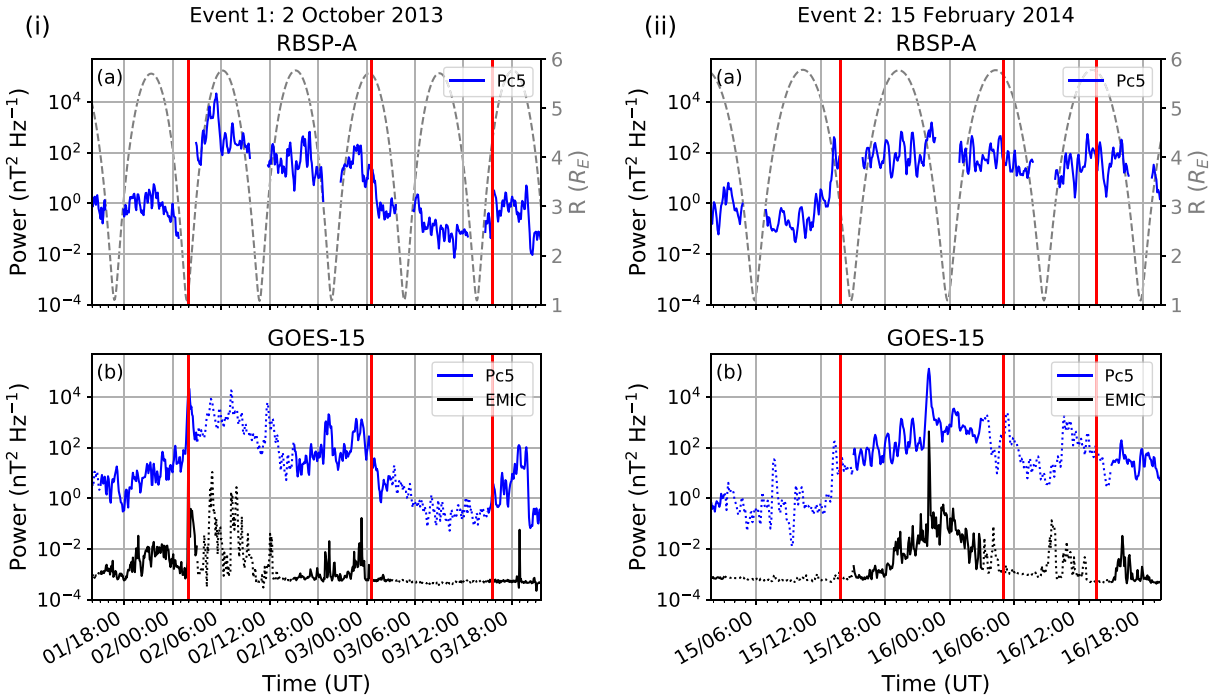

Figure 2. Ultra-low frequency (ULF) wave activity (i) on 2 Oct 2013 and (ii) on 15 Feb 2014. (a) Wave power of ULF Pc5 waves calculated with wavelet analysis from the magnitude of the magnetic field as measured by the EMFISIS instrument on Van Allen Probe A. The dashed gray line indicates the TS04D model spacecraft radial location. Wave power has been masked at $R < 3\ R_E$. (b) Wave power of ULF Pc5 and EMIC waves calculated with wavelet analysis from the magnitude of the magnetic field as measured by GOES-15. Solid and dotted lines indicate when the GOES spacecraft was on the dayside and nightside, respectively. The red vertical lines indicate the sheath and ICME ejecta intervals.

The ULF Pc5 wave power was very similar between GOES and Van Allen Probes observations, indicating that wave activity was present from geostationary orbit to the heart of the radiation belt at lower *L*-shells. The ULF Pc5 and EMIC wave power were elevated for Event 1 during the sheath region, and especially so in the front part of the sheath. The ULF Pc5 power decreased during the sheath, although it was elevated from pre-event levels throughout the sheath, and then quickly dropped during the ejecta. The EMIC power was low during most of the trailing part of the sheath and remained low during the ejecta. Event 2 also showed considerably elevated ULF Pc5 and EMIC power throughout the sheath, and ULF Pc5 power remained comparably elevated during the ejecta. The GOES observations show that the highest ULF Pc5 and EMIC wave power occurred at the center of the sheath when the dynamic pressure peaked. Similar results were measured by Van Allen Probe B and GOES-13 (see Figure S1).

The Van Allen Probes measured only a little chorus activity during both sheath events (shown for Van Allen Probe A in Figure S2). Based on the estimated plasmapause location, the stripes of enhanced emission extending to $>0.1 f_{ce}$ seen in the power spectra were likely plasmaspheric hiss, especially in Event 2. For both events (see Figure S2d), Van Allen Probes spent only a relatively short time on the dawnside, that is, between 0 and 12 UT, where the main chorus activity is expected to occur. To obtain a better estimate of the chorus activity, we investigated the chorus proxy based on Chen et al. (2014) and POES 30–100 keV electrons (see Section 2.2). These are shown in Figure 3 for both of our events.

The left panel of Figure 3 reveals that in Event 1 significant chorus wave activity was expected to occur in particular close to the shock and ejecta leading edges where the substorms occurred. According to the proxy, the chorus activity extended throughout the outer belt, from $L = 3.5$ to 9, and peaked at $L = 3.5$–4 just after the shock, that is, when the strongest substorm took place and *SYM-H* dipped. For Event 2, there was one interval of intense chorus close to the ejecta leading edge, again coinciding with the strongest substorm.

To summarize, both events caused significant Pc5 and EMIC activity, although wave activity peaked in different parts of the sheath region. The chorus activity was largely missed by the Van Allen Probes due to their orbit missing most of the dawnside, but the chorus proxy suggested that the more geoeffective Event 1 had in particular

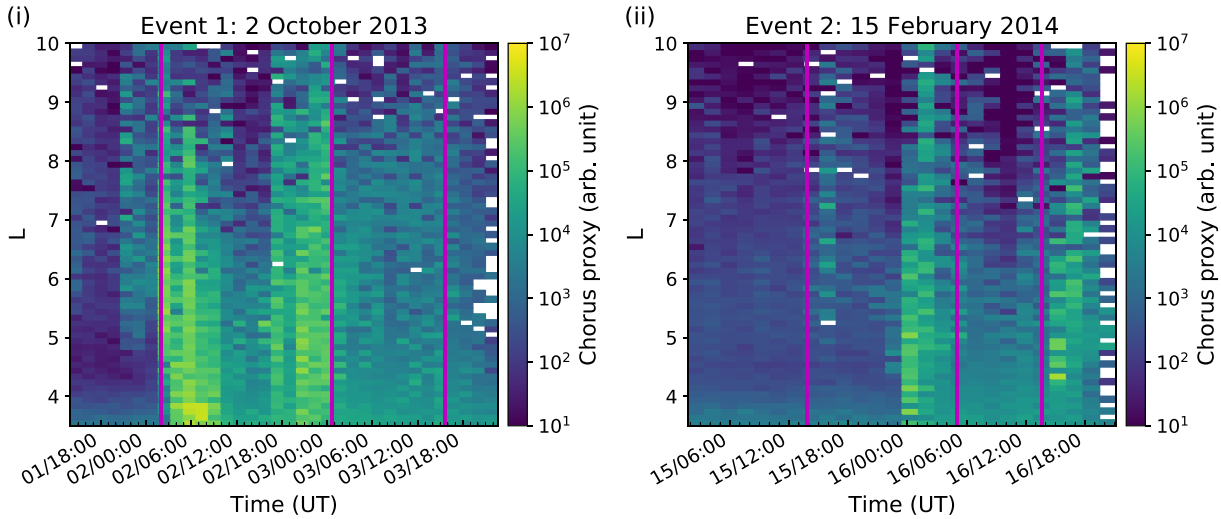

Figure 3. Chen et al. (2014) chorus proxy (with scaling factor $P = 1$) calculated from the geometric mean of the low-energy (30–100 keV) POES precipitating and trapped electron fluxes (a) for 2 October 2013 and (b) for 15 February 2014. The magenta vertical lines mark the sheath region and ICME ejecta intervals.

significant chorus wave activity. The chorus activity was less intense and hiss more intense in Event 2. These indicate the first event to be more conductive to produce enhancement of core electrons, while the second is more susceptible to prolonged depletion.

3.3. Electron Flux Observations

Electron fluxes from four Van Allen Probes energy channels representing the source, seed, core, and ultrarelativistic populations are presented in Figure 4. The data have been binned in 4 hr to make the main changes during the events readily identifiable, though the changes can appear more abrupt than they truly are. The solid and dashed lines in the top panels indicate the L-shell of the Van Allen Probes, pointing out the source of the binned data.

For Event 1, source and seed electrons were enhanced near the start of the sheath during the strong substorm activity. Source electron fluxes increased throughout the outer belt, but the strongest enhancement took place at $L = 3$–4. This is consistent with the chorus proxy in Figure 3 showing the peak at similar L range. Near the end of the sheath, during moderate substorm activity, the seed fluxes were further enhanced at $L > 4$. For Event 2, the background corrected electron flux data at source energies is not available, so we have shown the uncorrected fluxes instead. Contamination is not significant in this energy channel, so we expect the use of the uncorrected flux data to have minimal impact on the analysis. For Event 2, fluxes increased at source energies near the end of the sheath. Seed electrons were lightly enhanced at the shock, depleted near the end part of the sheath, and remained at about that depleted level during the ejecta. This is consistent with much weaker substorm activity during Event 2.

On the other hand, for Event 1 ultrarelativistic fluxes decreased soon after the start of the sheath while core fluxes remained at low values. The depletion occurred in two parts, first a stronger decrease on 2 October at ∼6 UT followed by a further depletion a bit later at ∼14 UT. A weak remnant belt however remained from the high pre-event fluxes at $L \sim 3$. Both the core and ultrarelativistic populations enhanced at $L > 4$ near the end of the sheath, similar to lower energies. For the highest energies, the remnant belt also intensified simultaneously, causing a clear two-part structure of the outer belt (Baker, Kanekal, Hoxie, Henderson, et al., 2013; Pinto et al., 2018).

For Event 2, similar to seed electrons, core electrons had a small enhancement at the shock. Ultrarelativistic electrons in turn experienced relatively strong enhancement at higher L-shells, with about an order of magnitude increase throughout $L > 4$. The band of the enhanced fluxes at MeV energies narrowed and moved to lower L-shells, and then depleted during the end part of the sheath simultaneously with the seed electrons. Again, no further significant changes were observed during the ejecta. For Event 2 the outer belt had a two-part structure at ultrarelativistic energies before the shock arrival that was destroyed during the sheath as the depleted fluxes at outer L-shells were not replenished, contrary to Event 1.

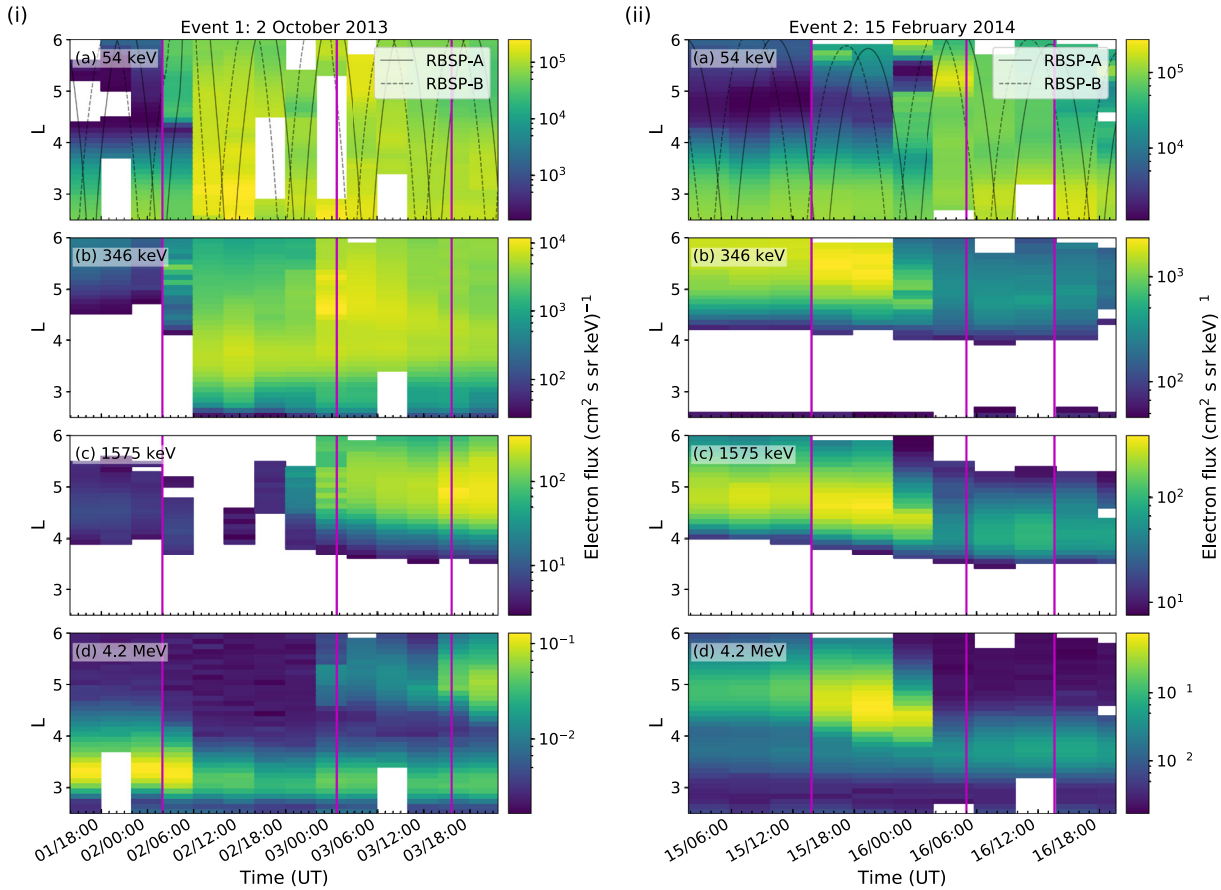

Figure 4. The spin-averaged electron fluxes measured by MagEIS at (a) 54 keV, (b) 346 keV, (c) 1,575 keV, and (d) by REPT at 4.2 MeV for the sheath events (i) on 2 October 2013 and (ii) on 15 February 2014. The data are combined from both Van Allen Probes and are binned by 4 hr in time and 0.1 in *L*-shell. The MagEIS electron fluxes are background corrected, except for the 54 keV fluxes in Event 2. The solid and dashed gray lines in the top panels indicate the orbits of Van Allen Probe A and B, respectively. The magenta vertical lines mark the sheath region and ICME ejecta intervals.

The overall response is given in Figure 5 in terms of the response parameter (Section 2.3) as a function of *L*-shell for the same four energy channels. This picture emphasizes the response to the sheath observed immediately after the sheath. First, Figure 5 highlights that for the geoeffective event (Event 1) the sheath enhanced fluxes from source to core energies at all *L*-shells investigated (i.e., values above the red dashed line), while for ultrarelativistic energies fluxes enhanced only at $L > 5$ and very slightly at $L < 3$. For the nongeoeffective event (Event 2), in turn, fluxes mostly stayed unchanged at $L < 4$ (or the background correction was unreliable) and depleted at $L > 4$, apart from source electrons which enhanced at $L > 4$. The deepest depletion occurred for ultrarelativistic electrons at $L \sim 5$ (i.e., contrary to the geoeffective event for which the fluxes enhanced at this part of the belt). We emphasize that the response parameter neglects the flux dynamics during the sheath, that is, it only concerns the result after the sheath relative to conditions before the sheath.

3.4. PSD Analysis Results

To gain more insight into acceleration and loss mechanisms during the investigated sheaths, we examined the electron observations using PSD. The results are shown in Figure 6 for Event 1 and Event 2 in the left and right hand panels, respectively. Two different values of magnetic moment μ are considered, $\mu = (300 \pm 10)$ MeV/G and $\mu = (3{,}000 \pm 100)$ MeV/G, and both have $K \leq 0.05\ R_E G^{1/2}$. The lower μ samples the seed and core populations, corresponding to about 500–800 keV at $L^* = 4$ and about 300–500 keV at $L^* = 5$ for both events. The larger μ samples the core and ultrarelativistic populations, corresponding to about 2.5–3 MeV (3–3.5 MeV) at $L^* = 4$ for Event 1 (Event 2) and about 1.5–2.5 MeV at $L^* = 5$ for both events. The energies and pitch angles corresponding to these μ and K ranges can be seen in more detail in the Supporting Information (Figures S3 and S4).

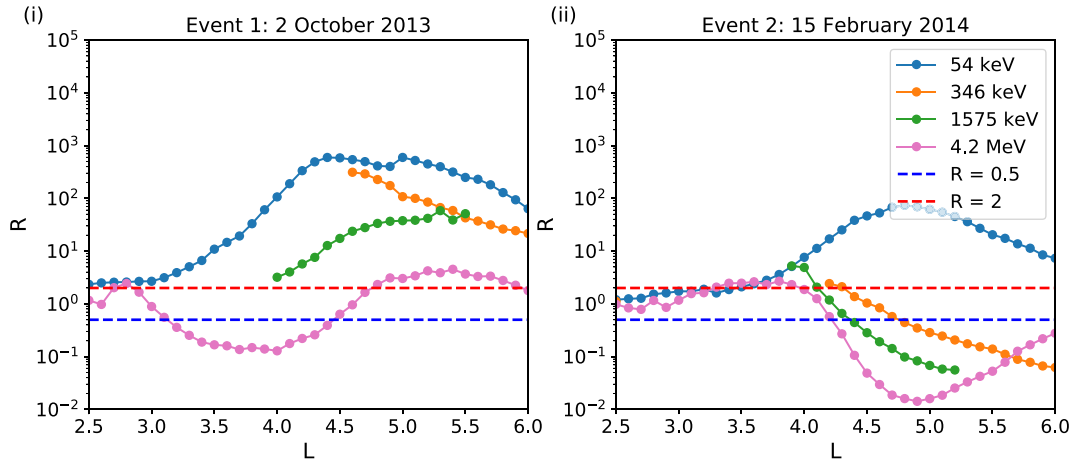

Figure 5. The response parameter (R) as a function of L-shell at four different energies representing the source (54 keV), seed (346 keV), core (1,575 keV), and ultrarelativistic (4.2 MeV) populations for the sheath events (a) on 2 October 2013 and (b) on 15 February 2014. The response parameter is defined as the ratio of electron flux averaged over 6 hr after and before the sheath region. The blue and red dashed lines show $R = 0.5$ and 2, respectively, indicating depletion ($R < 0.5$) and enhancement ($R > 2$) of electron fluxes due to the sheath region.

In Figure 6 showing the PSD profiles, squares and dots show the inbound orbits for Van Allen Probes A and B, respectively, and pluses and stars show the outbound orbits. The color coding from purple to yellow indicates the increasing time. Passes during which the shock (sheath start), the ejecta leading edge (sheath end), and the ejecta trailing edges occur are highlighted by labels. Videos highlighting the time evolution of PSD from pass to pass are available in the Supporting Information.

In agreement with electron fluxes discussed in the previous section, for Event 1 and for $\mu = 300$ MeV/G [Figure 6i(a)], PSD enhanced at $L^* > 3.8$. The first step of the enhancement occurred during the first half of the sheath, coinciding with the strong substorm activity, and resulted in a PSD increase of about two orders of magnitude in about one full orbit (9 hr, from purple to magenta curves). The PSD samples seed energies at $L^* \sim 5$, so the enhancement at high L^* was likely due to substorm injections of seed electrons. Subsequently, the injected seed electrons were likely accelerated to core energies, sampled at lower L^*, by a combination of local acceleration by chorus waves and inward radial diffusion driven by ULF waves. The activity of both of these wave modes was elevated during this time as measured in these L^* regions by both the POES proxy and the Van Allen Probes. No local peak is evident in these PSD profiles for this first step of enhancement, though it is possible that a peak for core electrons at $L^* \sim 4$ is concealed at higher L^* due to PSD sampling the increasing seed population further out. However, no peak at $L^* \sim 4$ is found while investigating other μ values (local peak at core energies at higher L^* is found with $\mu = 3{,}000$ MeV/G which is discussed below). To resolve a possible peak in the lower energies, observations beyond the Van Allen Probes apogee would be needed.

In the second step of the enhancement, PSD at $\mu = 300$ MeV/G increased by almost an order of magnitude at $L^* > 4$ during about 12 hr [magenta to orange curves in Figure 6i(a)] during the latter half of the sheath. The enhancement again coincided with substorm activity, indicating an increasing seed population due to substorm injections and an increasing source population at higher L^*. The chorus activity was again elevated at the time of the enhancement, but observations at higher L^* would be required to determine if the PSD profiles indicated a local peak formed by chorus acceleration at about 500 keV. The enhancement persisted for the duration of the sheath, after which the PSD slightly declined during the ejecta at $L^* > 4$ (orange to yellow curves).

On the other hand, in the front part of the sheath PSD for $\mu = 3{,}000$ MeV/G electrons in Event 1 [Figure 6i(b)] showed a decrease in PSD at $L^* > 4$, while the PSD increased at $L^* < 3$. This is a typical PSD signature of magnetopause shadowing losses due to combined magnetopause incursion and outward diffusion at higher L^*, and inward diffusion at lower L^* (e.g., Turner & Ukhorskiy, 2020). Later in the sheath and ejecta, PSD at $\mu = 3{,}000$ MeV/G increased considerably at around $L^* \sim 4$–5 and developed a peak, corresponding to 1.5–3 MeV core electrons. Electron fluxes at these energies present a larger enhancement than is seen for ultrarelativistic (4.2 MeV) electrons in Figure 4. The peak was first detected by Van Allen Probe A during its inbound pass

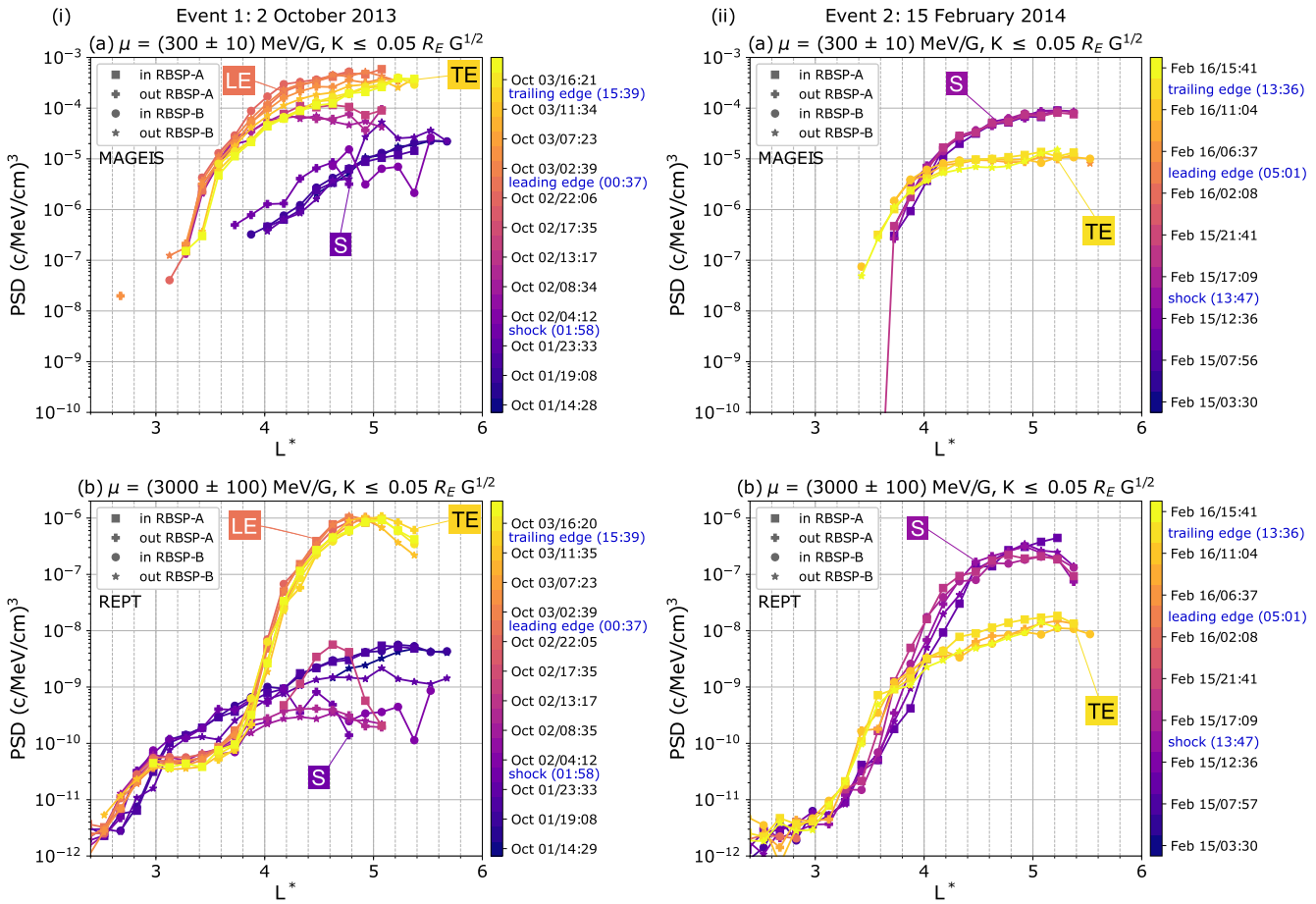

Figure 6. Phase Space Density (PSD) profiles (i) on 2 October 2013 and (ii) on 15 February 2014 representing nearly equatorially mirroring electrons with $K \leq 0.05$ $R_E G^{1/2}$. PSD versus L^* is shown for (a) seed and core energy particles (~600 keV at $L^* = 4$ and ~400 keV at $L^* = 5$) at $\mu = (300 \pm 10)$ MeV/G and (b) core and ultrarelativistic energy particles (~3 MeV at $L^* = 4$ and ~2 MeV at $L^* = 5$) at $\mu = (3{,}000 \pm 100)$ MeV/G. The profiles have been smoothed by averaging PSD to 0.15 L^* bins per pass. PSD calculations employed the TS04D magnetic field model and Van Allen Probes magnetic field measurements. The satellite passes are color-coded and the corresponding times are indicated in the color bar. The passes during the shock (S), ejecta leading edge (LE), and ejecta trailing edge (TE) are indicated. The inbound and outbound passes of RBSP-A and RBSP-B are shown with different markers as indicated in the legend.

starting at 15:25 UT on 2 October (magenta squares). PSD had increased by an order of magnitude compared to the earlier outbound pass. In the following inbound pass of Van Allen Probe A, starting at 00:10 UT on 3 October, the peak had increased by two orders of magnitude. That is, the peak grew three orders of magnitude in about 12 hr. The outbound pass of Van Allen Probe A between the peak growth observations of the inbound passes did not have PSD available at the considered μ and K ranges. Similarly, PSD was not available from Van Allen Probe B at the time of peak formation and growth, so we cannot confirm the local growing peak with a two-point measurement.

Nevertheless, we calculated the peak growth rate based on the Van Allen Probe A passes before, during and after peak growth [magenta pluses, magenta squares, and orange squares, respectively, in Figure 6i(b)]. We considered the three points at $L^* = 4.4$–4.8 at the peak location, and fitted a line to the logarithmic PSD values as a function of time for each of these L^* bins. The mean peak growth rate is 6.3 days^{-1} (i.e., orders of magnitude per day). The formation of this peak is discussed in detail in Section 4. After the peak growth observed by Van Allen Probe A, the peak was sustained at a similar level throughout the ejecta. The location of the peak also slowly drifted to higher L^* during the ejecta, from about $L^* = 4.6$ to 5. At this time, ULF Pc5 wave activity had decreased to pre-event levels, while the chorus proxy indicated some chorus activity that was lower than during the sheath. The chorus appeared to move toward higher L-shells during the ejecta, likely causing the outward drift of the peak.

Onward from the pass starting at 08:35 UT on 2 October, 6 hr after the shock, there appeared to be a dip in μ = 3,000 MeV/G PSD at $L^* \sim 3.3$ [Figure 6i(b)] which remained throughout the rest of the event, consistent with Figure 5 (pink curve for 4.2 MeV electrons). A local dip would be a signature of local loss, typically due to scattering by EMIC waves at ultrarelativistic energies. At the time of the appearance of the dip, there was some elevated EMIC activity [see Figure 2i(b)]. At L^* = 3–4, PSD with μ = 3,000 MeV/G and $K \leq 0.05\ R_E G^{1/2}$ corresponds to 70–90 deg pitch angles (see Figure S4). EMIC-driven losses favor lower pitch angles (Usanova et al., 2014), but the EMIC scattering is not negligible and can contribute to fast loss at near-equatorial pitch angles (Drozdov et al., 2019; Shprits et al., 2017).

For Event 2, Figure 6i(a) shows that PSD decreased about one order of magnitude at $L^* > 4$ in 13 hr (from the middle of the sheath to the middle of the ejecta) for μ = 300 MeV/G electrons which have mostly seed energies at this L^* range, evidencing magnetopause shadowing and outward diffusion. The PSD profiles also show an increase at $L^* < 4$ caused by inward radial diffusion, which is further evidence for magnetopause shadowing causing the electron dropout, as discussed above for Event 1. It is however unclear if the dropout in PSD at $L^* > 4$ is abrupt or gradual as no PSD data could be derived there at the chosen adiabatic invariant coordinates from 21:41 UT on 15 February to 08:43 UT on 16 February (i.e., the latter half of the sheath region where the dropout in electron fluxes is observed).

Similar PSD evolution took place for μ = 3,000 MeV/G electrons in Event 2 [Figure 6ii(b)]. There was about one order of magnitude decrease in PSD at $L^* > 4$ in 13 hr where the PSD samples the core population. PSD data is missing for the same time period as for μ = 300 MeV/G during the latter part of the sheath, indicating that the spacecraft were not measuring electrons in the chosen K range during this period. Similarly to μ = 300 MeV/G profiles, PSD increased at $L^* < 4$. Therefore, PSD signatures indicate again magnetopause shadowing losses due to combined magnetopause incursion and outward transport. At μ = 3,000 MeV/G, the inward radial diffusion was also already observed early in the sheath accompanied by decreasing PSD at the highest probed L^*, as opposed to PSD at μ = 300 MeV/G where increase at $L^* < 4$ was only observed during the ejecta. This indicates that magnetopause shadowing occurred throughout Event 2, for electrons at seed to core energies.

We have also investigated other μ ranges to assess the contribution of PSD sampling electrons at different energies at different L^*. The evolution these other μ ranges show is similar to the ones presented here. For example, PSD at $\mu = (1{,}000 \pm 40)$ MeV/G samples the higher and lower ends of the seed and core populations, respectively, corresponding to energies 0.7–1.7 MeV at $L^* > 4$. Its profiles show very similar evolution to the seed population captured by PSD at μ = 300 MeV/G in both events. PSD at $\mu = (5{,}000 \pm 170)$ MeV/G samples ultrarelativistic electrons (>3 MeV) below $L^* \sim 4.5$ and 2–3 MeV core electrons further out for Event 1. The PSD profiles present, similarly to PSD at μ = 3,000 MeV/G, first magnetopause shadowing losses at $L^* > 3$ and then a local peak at $L^* > 4$. For Event 2, PSD at μ = 5,000 MeV/G mainly samples the ultrarelativistic population with some contributions from the 2 to 3 MeV core population at $L^* \sim 5$. The PSD profiles, however, are essentially identical to the ones with PSD at μ = 3,000 MeV/G, showing magnetopause shadowing losses.

4. Discussion

The overall outer belt electron response, as shown by the response parameter (Figure 5), indicates opposite trends for the two investigated sheath regions. The geoeffective sheath caused a strong enhancement at all energies throughout the outer belt, except at L = 3–4.5 where ultrarelativistic electrons depleted. On the other hand, for the nongeoeffective event, depletion occurred from seed to ultrarelativistic energies at $L > 4$, while fluxes remained mostly unchanged at lower L-shells and the source population enhanced at $L > 4$.

It is however important to note that the overall response should be interpreted with caution as it does not take into account the variations within the sheath that can be significant. For example, the response parameter misses the strong enhancement at ultrarelativistic energies that occurred during the beginning of the sheath at L = 4–5 in the nongeoeffective event [Figure 4ii(d)] and only records the post-sheath depletion as compared to the pre-sheath levels. This initial brief enhancement was likely associated with the interplanetary shock impact that can quickly accelerate ultrarelativistic electrons via compression induced electric fields and drift resonant acceleration by related ULF waves (e.g., Hao et al., 2019; Kanekal et al., 2016). The response parameter calculated over short timescales (6 hr) nevertheless reveals the outer belt electron flux variation in response to specific driver

structures, as opposed to studies investigating considerably longer time periods (e.g., Reeves et al., 2003; Turner et al., 2015, 2019).

The analysis of electron fluxes and PSD for different Van Allen Probes orbits allowed for gaining more information of changes in the outer radiation belt during the sheaths and insight into processes that govern the electron dynamics. The behavior of seed and lower core energy electrons (PSD with $\mu = 300$ MeV/G; 300 keV to 1 MeV) during the sheath was drastically different between the two events. For Event 1, PSD at these energies enhanced at all probed L^*, while PSD during Event 2 enhanced only at lower L^* and decreased at higher L^*. As was mentioned in Section 3.4, the PSD behavior of $\mu = 300$ MeV/G electrons for Event 2 evidenced the effective magnetopause shadowing resulting from the combined process of magnetopause inward incursion and radial diffusion (Turner, Shprits, et al., 2012; Turner & Ukhorskiy, 2020). In addition, the most distinct variations of $\mu = 300$ MeV/G PSD occurred in different parts of the sheath for Events 1 and 2. These differences in the response at seed and core energies and timing of dynamics can be largely related to different levels of substorm activity and different solar wind dynamic pressure profiles that caused the magnetopause compression and ULF activity to peak in different parts of the sheath. The dynamic pressure, and consequentially the strongest magnetopause incursion and ULF Pc5 activity, occurred just after the shock in Event 1, while for Event 2 they occurred in the latter part of the sheath. Substorm injections producing a sufficiently enhanced seed population during Event 1 also enabled the subsequent enhancement at core energies (Boyd et al., 2016).

Seed and lower core energy electrons did not deplete at the start of the sheath in Event 1 despite the magnetopause incursion, as opposed to higher core and ultrarelativistic electrons (PSD with $\mu = 3{,}000$ MeV/G; 1.5–5 MeV). This could be related to strong substorm activity quickly replenishing lower energy electrons and to their slower drift times about the Earth (from tens of minutes to more than an hour, compared to minutes for ultrarelativistic electrons in the heart of the belt) combined with the briefness of the strongest magnetopause compression.

The significant PSD enhancement at $\mu = 300$ MeV/G, which occurred in two steps, is likely related to strong substorm activity continuing injecting electrons, and fast ULF wave driven inward radial diffusion, as well as the magnetopause relaxing toward a more nominal position. Van Allen Probes measurements of ULF Pc5 waves confirmed elevated wave activity in the heart of the outer belt during the sheath region when the strong enhancements in PSD occurred. Since the chorus proxy also indicated elevated chorus activity during both steps of enhancement, local chorus acceleration likely contributed to energizing the seed population, even though a local peak cannot be identified in the PSD profiles for the lower energy core population (as opposed to the higher energy core population sampled by PSD at $\mu = 3{,}000$ MeV/G). The evolution of the PSD gradient especially during the latter part of the sheath suggests the existence of an increasing source population at higher L^* (Chen, Reeves, & Friedel, 2007).

We note that the level of magnetopause compression and ULF wave activity was similar between the two events. The geoeffective event however resulted in significant substorm injections and a growing source population at high L^* that dominated over losses at the magnetopause and led to a drastically different response of $\mu = 300$ MeV/G electrons as compared to the nongeoeffective event.

Core and ultrarelativistic electron PSD ($\mu = 3{,}000$ MeV/G) showed also very distinct responses between the studied events. For Event 2, core and ultrarelativistic electrons responded very similarly to the electrons at lower energies, that is, the response evidenced effective magnetopause shadowing. The initial strong enhancement at ultrarelativistic energies seen in the electron fluxes is not noticeable in the PSD profiles [Figure 6ii(b)] due to the lack of PSD measurements at $L^* > 4$ before the enhancement. The PSD profiles for Event 1 presented also a similar loss process during the closest magnetopause incursion just after the shock, but the geoeffective event experienced a very different response during the latter part of the sheath and ejecta, as described below. We note that the solar wind conditions in Event 1 follow the three criteria of Li et al. (2015) for efficient MeV electron acceleration: prolonged southward Bz (several hours), high solar wind speed ($>\sim$500 kms^{-1}), and low dynamic pressure ($<\sim$2 nPa). PSD enhanced only after the dynamic pressure dropped to low values during the latter part of the sheath. The drop in dynamic pressure allowed the magnetopause to move outward, leading to decreased magnetopause shadowing losses. On the other hand, the elevated dynamic pressure throughout the sheath of Event 2 caused persistent losses via magnetopause shadowing.

A particularly distinct feature for core electrons at $\mu = 3{,}000$ MeV/G PSD for Event 1 is the development of a peak. A local peak is usually taken as evidence for local acceleration by chorus waves. The chorus proxy suggests

these waves were present throughout the sheath, and the activity also intensified at the time when the peak grew strongly. The chorus activity was spread along a wide range of L, but was strongest around the radial location of the PSD peak. The peak was observed at $L^* = 4.6$–5 and it appeared near the middle of the sheath. The peak grew three orders of magnitude in ∼12 hr. Local peaks near $L^* = 4$–5 have been commonly observed in previous studies (e.g., Green & Kivelson, 2004; Kanekal et al., 2015; Li et al., 2014, 2016; Reeves et al., 2013; Turner, Angelopoulos, Li, et al., 2014). Similar peak growth rate as in our study was observed by Reeves et al. (2013), which was interpreted to have arisen due to local acceleration by chorus waves by Thorne et al. (2013). Slower growth rates of about two orders of magnitude in ∼12 hr and about four orders of magnitude in ∼2 days were observed by Li et al. (2014, 2016), respectively, and both concluded using diffusion simulations that chorus was the dominant cause for acceleration to MeV energies.

There is some ambiguity for the mechanism generating the PSD peak in Event 1 due to the limited Van Allen Probes measurements beyond $L^* = 5$, and due to peak growth solely recorded by a single pass of Van Allen Probe A without confirmation from Van Allen Probe B. However, the existence of a local peak in Event 1 at similar energies has been confirmed by THEMIS spacecraft measurements beyond Van Allen Probes apogee by Boyd et al. (2018), who also found local acceleration to be the typical cause for energization at MeV energies. This confirmation of a local peak, the elevated chorus activity shown by the proxy, and similar growth rate to previous studies discussed above, combined with strong substorm activity during the sheath, strongly suggest that substorm-injected seed electrons (seen in PSD with $\mu = 300$ MeV/G) were accelerated to 1.5–3 MeV core energies by chorus waves locally at $L^* = 4$–5. In addition, since the peak retained its shape and magnitude for at least 12 hr, there must be an active source to balance the ULF-driven radial diffusion that would flatten and broaden the peak. This would be from local acceleration or a sustained source of electrons further out, but there are no indication of inward radial diffusion that would support the latter explanation. Instead, the peak is slowly transported outwards during the ejecta which is consistent with typical recovery where chorus acceleration moves to higher L-shells.

There is another interesting feature in the PSD profiles of the geoeffective event at $\mu = 3{,}000$ MeV/G: a dip-like decrease in PSD at $L^* = 3$–3.6, which suggest a local loss. Considering the electron fluxes, the strongest depletion of the ultrarelativistic population at low L ($L \sim 3.5$) occurred sometime between 4 and 7 UT on 2 October when both Van Allen Probes moved from inside to outside the plasmasphere. Such depletions at low L for ultrarelativistic energies are commonly reported in previous studies (e.g., Aseev et al., 2017; Turner, Angelopoulos, Li, et al., 2014; Turner, Angelopoulos, Morley, et al., 2014; Turner et al., 2013), but their causes have remained uncertain. The depletion occurred during the front part of the sheath when the inner magnetospheric wave activity was intense (Pc5, EMIC, chorus, and hiss waves). Fast losses at ultrarelativistic energies accompanied with dips in PSD profiles have been reported to be caused by EMIC wave interactions (Aseev et al., 2017; Shprits et al., 2017). Analysis of pitch angle resolved multi-MeV fluxes showed that depletion consistent with EMIC-driven losses occurs also at the near-equatorial (75°) pitch angles (Drozdov et al., 2019), which are sampled by our PSD. The local dip in PSD at ultrarelativistic energies can thus indicate losses by EMIC wave scattering, perhaps in concert with pitch angle diffusion by hiss or chorus waves. The EMIC-driven loss can be as fast as hours for the ultrarelativistic population (e.g., Kurita et al., 2018). Another mechanism that has been invoked to deplete ultrarelativistic fluxes quickly throughout the outer belt is the combined effect of magnetopause incursion, ULF wave transport, and drift-shell splitting (Zhang et al., 2016). Since the dip in PSD did not deepen considerably during the event, we also consider the possibility that a dip-like feature arose from a combination of overall loss and subsequent energization at core energies. Magnetopause shadowing due to magnetopause inward incursion and ULF-driven outward diffusion could have progressed to deplete ultrarelativistic energies at $L^* = 3$–4, while elevated chorus activity could have already started to accelerate electrons to core energies seen at $L^* > 4$.

It is also interesting to note that a three-part radiation belt structure for ultrarelativistic electrons (4.2 MeV, Figure 4) was created as a response to the sheath region of the geoeffective event, that is, the outer belt split into two parts (Baker, Kanekal, Hoxie, Batiste, et al., 2013; Pinto et al., 2018; Turner et al., 2013). For the nongeoeffective event, in turn, a pre-existing two-part outer belt structure disappeared leaving only the remnant belt. For the geoeffective event, part of the intense remnant belt, which was present before the shock arrival, remained through the sheath despite suffering a considerable depletion at the start of the sheath and a further smaller depletion during the trailing part of the sheath. The largest L-shells of the outer belt captured by Van Allen Probes were largely devoid of ultrarelativistic electrons from the pre-event until the end of the sheath, after which

fresh ultrarelativistic electrons appeared. The region $L \sim 4$ remained however devoid of electrons producing the two-part outer belt structure. For the nongeoeffective event, the disappearance of a two-part outer belt structure was caused by two processes, as indicated by the PSD analysis. First, ULF wave related inward transport filled the existing gap between the two bands of enhanced fluxes (remnant belt at $L = 3.5$–4 and an outer belt at $L > 4.5$) that were present before the event. Second, electrons were removed from high L-shells by magnetopause shadowing and outward transport by ULF waves without much further energization, leaving only the remnant belt.

This study highlights that regions close to the shock and ejecta leading edge seem to be key periods when changes in the radiation belt system occur, including most enhanced precipitation from the radiation belts. The major variations of outer belt electron fluxes, both depletion and enhancement, were observed under the influence of these regions. The statistical study of Kalliokoski et al. (2020) showed that the *AL* index dips after the shock for all sheath events and dips close to the ejecta leading edge for all geoeffective sheaths, indicating intense substorm activity in these key regions. Kilpua et al. (2019) similarly found that regions near the start and end of a sheath are the most geoeffective. These regions also exhibit enhanced ULF wave activity (Kilpua et al., 2013).

Additionally, this study indicated that the chorus proxy based on electron precipitation was important for capturing the chorus wave activity. For both of the studied events, the Van Allen Probes spent little time in the dawn sector where chorus waves typically occur. The chorus proxy also allowed estimation of the L-range of chorus activity showing that it encompassed the entire outer radiation belt. Some chorus activity was almost continuous throughout the geoeffective event, but the activity peaked strongly in the above described key sheath sub-regions: just after the shock and close to the ejecta leading edge. This is consistent with strong disturbances in the *AL* index at these times, indicating large substorm activity that would likely generate chorus waves and provide a seed population for core and ultrarelativistic growth via local chorus acceleration (Jaynes et al., 2015; Miyoshi et al., 2013). These sub-regions showed also the strongest chorus activity for the nongeoffective event.

5. Conclusions

We studied the effects of two ICMEs with sheath regions on the outer radiation belt electrons. The two sheath events were geoeffective (2 October 2013; Event 1) and nongeoeffective (15 February 2014; Event 2) based on the *SYM-H* geomagnetic activity index during the sheath, and neither ejecta caused significant geomagnetic disturbances.

Our study highlights that both geoeffective and nongeoeffective drivers caused drastic variations of the outer radiation belt electron fluxes up to ultrarelativistic energies. The overall response of the outer belt to the sheath for the geoeffective and nongeoeffective sheaths were the opposite: the geoeffective event led to enhancement for most of the energies and L-ranges, while the nongeoeffective event mainly resulted in depletion. The overall response for a given event however hides some distinct variations. For example, for the nongeoeffective event ultrarelativistic electrons experienced about an order of magnitude increase during the sheath before they depleted.

Analysis of electron PSD at seed, core, and ultrarelativistic energies showed that the enhancements observed during the geoeffective sheath were likely due to substorm injections at seed energies and local acceleration by chorus waves at core energies. In both events, depletion predominantly occurred via loss to the magnetopause driven by magnetopause compression and outward transport by ULF waves. These different responses derive from differences in substorm activity during the events and the properties of the two sheaths. The different timing and extent of the solar wind dynamic pressure pulse in the sheath contributed to the timing of the closest magnetopause inward incursion and thus when magnetopause shadowing losses were dominant. The relaxation of the magnetopause early in the geoeffective sheath along with mostly southward IMF, leading to stronger substorm activity that generated chorus waves, created favorable conditions for energization of core and ultrarelativistic electrons, as opposed to the nongeoeffective sheath.

The results revealed the importance of ULF wave driven inward and outward radial transport for governing electron dynamics, together with the compression of the magnetopause. Combining GOES and Van Allen Probes ULF Pc5 wave observations showed that the activity of these waves was elevated during the sheath regions not only near the geostationary orbit but also in the heart of the outer radiation belt. Local acceleration by chorus waves caused the strongest enhancement at core energies, and the chorus proxy from POES satellites' precipitation measurements was integral in confirming this energization process.

We also noted the existence of key sheath sub-regions, located at the start and end of the sheath (i.e., near the shock and ejecta leading edge), where the main variations in the radiation belt system occur. An interesting difference between the events was that the geoeffective sheath created a two-part outer belt structure, while the nongeoeffective sheath destroyed such pre-existing configuration.

Additional case studies are needed to determine if there are repeatable patterns in the response processes of the radiation belt system to sheaths. A statistical approach to PSD analysis could shed light on the dominant electron dynamics (e.g., Murphy et al., 2018; Nasi et al., 2020; Turner et al., 2017; Zhao et al., 2019). Future work will target events after August 2015 when data from the Magnetospheric Multiscale Mission (MMS) is available. The orbit of MMS allows investigation of PSD distributions beyond Van Allen Probes apogee eliminating the ambiguity of PSD gradients near geosynchronous orbit (e.g., Cohen et al., 2021).

Data Availability Statement

The authors are thankful to all of the Van Allen Probes, Wind, and OMNI teams for making their data available to the public. The OMNI and Wind data were obtained through CDAWeb (https://cdaweb.sci.gsfc.nasa.gov/index.html/). We thank Harlan Spence and the ECT team for Van Allen Probes MagEIS and REPT electron flux data (https://rbsp-ect.newmexicoconsortium.org/science/DataDirectories.php) and Craig Kletzing and the EMFISIS team for Van Allen Probes wave data (https://emfisis.physics.uiowa.edu/data/index). POES data is available through NOAA (https://www.ngdc.noaa.gov/stp/satellite/poes/dataaccess.html) and we thank Timo Asikainen for providing the processed POES data which were obtained through the PROSPECT project (Academy of Finland Grant 321440).

Acknowledgments
The results presented here have been achieved under the framework of the Finnish Centre of Excellence in Research of Sustainable Space (Academy of Finland Grant 1312390), which we gratefully acknowledge. Emilia K. J. Kilpua acknowledges the European Research Council (ERC) under the European Union's Horizon 2020 Research and Innovation Programme Project SolMAG 724391, and Academy of Finland project 1310445. The work of Lucile Turc is supported by the Academy of Finland (Grant 322544). Minna Palmroth acknowledges ERC under the European Union's Horizon 2020 Research and Innovation Programme Project 682068-PRESTISSIMO, and Academy of Finland project 312351.

References

Alves, L. R., Da Silva, L. A., Souza, V. M., Sibeck, D. G., Jauer, P. R., Vieira, L. E. A., et al. (2016). Outer radiation belt dropout dynamics following the arrival of two interplanetary coronal mass ejections. *Geophysical Research Letters*, *43*, 978–987. https://doi.org/10.1002/2015GL067066

Anderson, B. R., Millan, R. M., Reeves, G. D., & Friedel, R. H. W. (2015). Acceleration and loss of relativistic electrons during small geomagnetic storms. *Geophysical Research Letters*, *42*(23), 10113–10119. https://doi.org/10.1002/2015GL066376

Aseev, N. A., Shprits, Y. Y., Drozdov, A. Y., Kellerman, A. C., Usanova, M. E., Wang, D., & Zhelavskaya, I. S. (2017). Signatures of ultrarelativistic electron loss in the heart of the outer radiation belt measured by Van Allen Probes. *Journal of Geophysical Research: Space Physics*, *122*(10), 10102–10111. https://doi.org/10.1002/2017JA024485

Asikainen, T. (2017). Calibrated and corrected POES/MEPED energetic particle observations. In A. Belehaki, M. Hapgood, & J. Watermann (Eds.), *The ESPAS e-infrastructure: Access to data in near-Earth space* (pp. 57–69). EDPSciences. https://doi.org/10.1051/978-2-7598-1949-2

Asikainen, T., & Mursula, K. (2013). Correcting the NOAA/MEPED energetic electron fluxes for detector efficiency and proton contamination. *Journal of Geophysical Research: Space Physics*, *118*(10), 6500–6510. https://doi.org/10.1002/jgra.50584

Baker, D. N., Kanekal, S. G., Hoxie, V. C., Batiste, S., Bolton, M., Li, X., et al. (2013). The relativistic electron-proton telescope (REPT) instrument on board the radiation belt storm probes (RBSP) spacecraft: Characterization of Earth's radiation belt high-energy particle populations. *Space Science Reviews*, *179*(1–4), 337–381. https://doi.org/10.1007/s11214-012-9950-9

Baker, D. N., Kanekal, S. G., Hoxie, V. C., Henderson, M. G., Li, X., Spence, H. E., et al. (2013). A long-lived relativistic electron storage ring embedded in Earth's outer Van Allen belt. *Science*, *340*(6129), 186–190. https://doi.org/10.1126/science.1233518

Blake, J. B., Carranza, P. A., Claudepierre, S. G., Clemmons, J. H., Crain, W. R., Dotan, Y., et al. (2013). The Magnetic Electron Ion Spectrometer (MagEIS) instruments aboard the radiation belt storm probes (RBSP) spacecraft. *Space Science Reviews*, *179*(1–4), 383–421. https://doi.org/10.1007/s11214-013-9991-8

Bortnik, J., & Thorne, R. M. (2007). The dual role of ELF/VLF chorus waves in the acceleration and precipitation of radiation belt electrons. *Journal of Atmospheric and Solar-Terrestrial Physics*, *69*(3), 378–386. https://doi.org/10.1016/j.jastp.2006.05.030

Boyd, A. J., Reeves, G. D., Spence, H. E., Funsten, H. O., Larsen, B. A., Skoug, R. M., et al. (2019). RBSP-ECT combined spin-averaged electron flux data product. *Journal of Geophysical Research: Space Physics*, *124*(11), 9124–9136. https://doi.org/10.1029/2019JA026733

Boyd, A. J., Spence, H. E., Claudepierre, S. G., Fennell, J. F., Blake, J. B., Baker, D. N., et al. (2014). Quantifying the radiation belt seed population in the 17 March 2013 electron acceleration event. *Geophysical Research Letters*, *41*(7), 2275–2281. https://doi.org/10.1002/2014GL059626

Boyd, A. J., Spence, H. E., Huang, C. L., Reeves, G. D., Baker, D. N., Turner, D. L., et al. (2016). Statistical properties of the radiation belt seed population. *Journal of Geophysical Research: Space Physics*, *121*(8), 7636–7646. https://doi.org/10.1002/2016JA022652

Boyd, A. J., Turner, D. L., Reeves, G. D., Spence, H. E., Baker, D. N., & Blake, J. B. (2018). What causes radiation belt enhancements: A survey of the Van Allen Probes era. *Geophysical Research Letters*, *45*(11), 5253–5259. https://doi.org/10.1029/2018GL077699

Burtis, W. J., & Helliwell, R. A. (1969). Banded chorus—A new type of VLF radiation observed in the magnetosphere by OGO 1 and OGO 3. *Journal of Geophysical Research*, *74*(11), 3002. https://doi.org/10.1029/JA074i011p03002

Chen, Y., Friedel, R. H. W., Reeves, G. D., Cayton, T. E., & Christensen, R. (2007). Multisatellite determination of the relativistic electron phase space density at geosynchronous orbit: An integrated investigation during geomagnetic storm times. *Journal of Geophysical Research: Space Physics*, *112*(A11), A11214. https://doi.org/10.1029/2007JA012314

Chen, Y., Friedel, R. H. W., Reeves, G. D., Onsager, T. G., & Thomsen, M. F. (2005). Multisatellite determination of the relativistic electron phase space density at geosynchronous orbit: Methodology and results during geomagnetically quiet times. *Journal of Geophysical Research: Space Physics*, *110*(A10), A10210. https://doi.org/10.1029/2004JA010895

Chen, Y., Reeves, G. D., & Friedel, R. H. W. (2007). The energization of relativistic electrons in the outer Van Allen radiation belt. *Nature Physics*, *3*(9), 614–617. https://doi.org/10.1038/nphys655

Chen, Y., Reeves, G. D., Friedel, R. H. W., & Cunningham, G. S. (2014). Global time-dependent chorus maps from low-Earth-orbit electron precipitation and Van Allen Probes data. *Geophysical Research Letters*, *41*(3), 755–761. https://doi.org/10.1002/2013GL059181

Claudepierre, S. G., O'Brien, T. P., Blake, J. B., Fennell, J. F., Roeder, J. L., Clemmons, J. H., et al. (2015). A background correction algorithm for Van Allen Probes MagEIS electron flux measurements. *Journal of Geophysical Research: Space Physics*, *120*(7), 5703–5727. https://doi.org/10.1002/2015JA021171

Cohen, I. J., Turner, D. L., Michael, A. T., Sorathia, K. A., & Ukhorskiy, A. Y. (2021). Investigating the link between outer radiation belt losses and energetic electron escape at the magnetopause: A case study using multi-mission observations and simulations. *Journal of Geophysical Research: Space Physics*, *126*(6), e2021JA029261. https://doi.org/10.1029/2021JA029261

Da Silva, L. A., Shi, J., Alves, L. R., Sibeck, D., Souza, V. M., Marchezi, J. P., et al. (2020). Dynamic mechanisms associated with high-energy electron flux dropout in the Earth's outer radiation belt under the influence of a coronal mass ejection sheath region. *Journal of Geophysical Research: Space Physics*, *126*(1), e2020JA028492. https://doi.org/10.1029/2020JA028492

Daglis, I. A., Katsavrias, C., & Georgiou, M. (2019). From solar sneezing to killer electrons: Outer radiation belt response to solar eruptions. *Philosophical Transactions of the Royal Society A*, *377*(2148), 20180097. https://doi.org/10.1098/rsta.2018.0097

Drozdov, A. Y., Aseev, N., Effenberger, F., Turner, D. L., Saikin, A., & Shprits, Y. Y. (2019). Storm time depletions of multi-MeV radiation belt electrons observed at different pitch angles. *Journal of Geophysical Research: Space Physics*, *124*(11), 8943–8953. https://doi.org/10.1029/2019JA027332

Engebretson, M. J., Posch, J. L., Braun, D. J., Li, W., Ma, Q., Kellerman, A. C., et al. (2018). EMIC wave events during the four GEM QARBM challenge intervals. *Journal of Geophysical Research: Space Physics*, *123*(8), 6394–6423. https://doi.org/10.1029/2018JA025505

Evans, D. S., & Greer, M. S. (2004). *Polar orbiting environmental satellite space environment monitor – 2: Instrument descriptions and archive data documentation* (Technical Report No. version 1.4). Space Environment Center.

George, H., Kilpua, E., Osmane, A., Asikainen, T., Kalliokoski, M. M. H., Rodger, C. J., et al. (2020). Outer Van Allen belt trapped and precipitating electron flux responses to two interplanetary magnetic clouds of opposite polarity. *Annales Geophysicae*, *38*(4), 931–951. https://doi.org/10.5194/angeo-38-931-2020

Georgiou, M., Daglis, I. A., Rae, I. J., Zesta, E., Sibeck, D. G., Mann, I. R., et al. (2018). Ultralow frequency waves as an intermediary for solar wind energy input into the radiation belts. *Journal of Geophysical Research: Space Physics*, *123*(12), 10090–10108. https://doi.org/10.1029/2018JA025355

Gonzalez, W. D., Joselyn, J. A., Kamide, Y., Kroehl, H. W., Rostoker, G., Tsurutani, B. T., & Vasyliunas, V. M. (1994). What is a geomagnetic storm? *Journal of Geophysical Research*, *99*(A4), 5771–5792. https://doi.org/10.1029/93JA02867

Green, J. C. (2006). Using electron phase space density signatures to identify the electromagnetic waves responsible for accelerating relativistic electrons in Earth's magnetosphere. In K. Takahashi, P. J. Chi, R. E. Denton, & R. L., Lysak, (Eds.), *Magnetospheric ULF waves: Synthesis and new directions* (Vol. 169, p. 225). American Geophysical Union. https://doi.org/10.1029/169GM15

Green, J. C., & Kivelson, M. G. (2001). A tale of two theories: How the adiabatic response and ULF waves affect relativistic electrons. *Journal of Geophysical Research*, *106*(A11), 25777–25792. https://doi.org/10.1029/2001JA000054

Green, J. C., & Kivelson, M. G. (2004). Relativistic electrons in the outer radiation belt: Differentiating between acceleration mechanisms. *Journal of Geophysical Research: Space Physics*, *109*(A3), A03213. https://doi.org/10.1029/2003JA010153

Hao, Y. X., Zong, Q. G., Zhou, X. Z., Rankin, R., Chen, X. R., Liu, Y., et al. (2019). Global-scale ULF waves associated with SSC accelerate magnetospheric ultrarelativistic electrons. *Journal of Geophysical Research: Space Physics*, *124*(3), 1525–1538. https://doi.org/10.1029/2018JA026134

Hargreaves, J. K., Birch, M. J., & Evans, D. S. (2010). On the fine structure of medium energy electron fluxes in the auroral zone and related effects in the ionospheric D-region. *Annales Geophysicae*, *28*(5), 1107–1120. https://doi.org/10.5194/angeo-28-1107-2010

Hartley, D. P., & Denton, M. H. (2014). Solving the radiation belt riddle. *Astronomy and Geophysics*, *55*(6), 617–620. https://doi.org/10.1093/astrogeo/atu247

Hietala, H., Kilpua, E. K. J., Turner, D. L., & Angelopoulos, V. (2014). Depleting effects of ICME-driven sheath regions on the outer electron radiation belt. *Geophysical Research Letters*, *41*(7), 2258–2265. https://doi.org/10.1002/2014GL059551

Jacobs, J. A., Kato, Y., Matsushita, S., & Troitskaya, V. A. (1964). Classification of geomagnetic micropulsations. *Journal of Geophysical Research*, *69*(1), 180–181. https://doi.org/10.1029/JZ069i001p00180

Jaynes, A. N., Baker, D. N., Singer, H. J., Rodriguez, J. V., Loto'aniu, T. M., Ali, A. F., et al. (2015). Source and seed populations for relativistic electrons: Their roles in radiation belt changes. *Journal of Geophysical Research: Space Physics*, *120*(9), 7240–7254. https://doi.org/10.1002/2015JA021234

Kalliokoski, M. M. H., Kilpua, E. K. J., Osmane, A., Turner, D. L., Jaynes, A. N., Turc, L., et al. (2020). Outer radiation belt and inner magnetospheric response to sheath regions of coronal mass ejections: A statistical analysis. *Annales Geophysicae*, *38*(3), 683–701. https://doi.org/10.5194/angeo-38-683-2020

Kanekal, S. G., Baker, D. N., Fennell, J. F., Jones, A., Schiller, Q., Richardson, I. G., et al. (2016). Prompt acceleration of magnetospheric electrons to ultrarelativistic energies by the 17 March 2015 interplanetary shock. *Journal of Geophysical Research: Space Physics*, *121*(8), 7622–7635. https://doi.org/10.1002/2016JA022596

Kanekal, S. G., Baker, D. N., Henderson, M. G., Li, W., Fennell, J. F., Zheng, Y., et al. (2015). Relativistic electron response to the combined magnetospheric impact of a coronal mass ejection overlapping with a high-speed stream: Van Allen Probes observations. *Journal of Geophysical Research: Space Physics*, *120*(9), 7629–7641. https://doi.org/10.1002/2015JA021395

Kataoka, R., & Miyoshi, Y. (2006). Flux enhancement of radiation belt electrons during geomagnetic storms driven by coronal mass ejections and corotating interaction regions. *Space Weather*, *4*(9), 09004. https://doi.org/10.1029/2005SW000211

Katsavrias, C., Daglis, I. A., Turner, D. L., Sand berg, I., Papadimitriou, C., Georgiou, M., & Balasis, G. (2015). Nonstorm loss of relativistic electrons in the outer radiation belt. *Geophysical Research Letters*, *42*(24), 10521–10530. https://doi.org/10.1002/2015GL066773

Kilpua, E. K. J., Balogh, A., von Steiger, R., & Liu, Y. D. (2017). Geoeffective properties of solar transients and stream interaction regions. *Space Science Reviews*, *212*, 1271–1314. https://doi.org/10.1007/s11214-017-0411-3

Kilpua, E. K. J., Fontaine, D., Moissard, C., Ala-Lahti, M., Palmerio, E., Yordanova, E., et al. (2019). Solar wind properties and geospace impact of coronal mass ejection-driven sheath regions: Variation and driver dependence. *Space Weather*, *17*(0). https://doi.org/10.1029/2019SW002217

Kilpua, E. K. J., Hietala, H., Koskinen, H. E. J., Fontaine, D., & Turc, L. (2013). Magnetic field and dynamic pressure ULF fluctuations in coronal-mass-ejection-driven sheath regions. *Annales Geophysicae*, *31*(9), 1559–1567. https://doi.org/10.5194/angeo-31-1559-2013

Kilpua, E. K. J., Hietala, H., Turner, D. L., Koskinen, H. E. J., Pulkkinen, T. I., Rodriguez, J. V., et al. (2015). Unraveling the drivers of the storm time radiation belt response. *Geophysical Research Letters*, *42*(9), 3076–3084. https://doi.org/10.1002/2015GL063542

Kilpua, E. K. J., Koskinen, H. E. J., & Pulkkinen, T. I. (2017). Coronal mass ejections and their sheath regions in interplanetary space. *Living Reviews in Solar Physics*, *14*(1), 5. https://doi.org/10.1007/s41116-017-0009-6

Kim, H.-J., & Chan, A. A. (1997). Fully adiabatic changes in storm time relativistic electron fluxes. *Journal of Geophysical Research*, *102*(A10), 22107–22116. https://doi.org/10.1029/97JA01814

Kletzing, C. A., Kurth, W. S., Acuna, M., MacDowall, R. J., Torbert, R. B., Averkamp, T., et al. (2013). The electric and magnetic field instrument suite and integrated science (EMFISIS) on RBSP. *Space Science Reviews*, *179*(1–4), 127–181. https://doi.org/10.1007/s11214-013-9993-6

Koons, H. C., & Roeder, J. L. (1990). A survey of equatorial magnetospheric wave activity between 5 and 8 R_E. *Planetary and Space Science*, *38*(10), 1335–1341. https://doi.org/10.1016/0032-0633(90)90136-E

Kurita, S., Miyoshi, Y., Shiokawa, K., Higashio, N., Mitani, T., Takashima, T., et al. (2018). Rapid loss of relativistic electrons by EMIC waves in the outer radiation belt observed by Arase, Van Allen Probes, and the PWING ground stations. *Geophysical Research Letters*, *45*(23), 12720–12729. https://doi.org/10.1029/2018GL080262

Kurth, W. S., De Pascuale, S., Faden, J. B., Kletzing, C. A., Hospodarsky, G. B., Thaller, S., & Wygant, J. R. (2015). Electron densities inferred from plasma wave spectra obtained by the Waves instrument on Van Allen Probes. *Journal of Geophysical Research: Space Physics*, *120*(2), 904–914. https://doi.org/10.1002/2014JA020857

Lam, M. M., Horne, R. B., Meredith, N. P., Glauert, S. A., Moffat-Griffin, T., & Green, J. C. (2010). Origin of energetic electron precipitation >30 keV into the atmosphere. *Journal of Geophysical Research: Space Physics*, *115*(8), A00F08. https://doi.org/10.1029/2009JA014619

Lepping, R. P., Acũna, M. H., Burlaga, L. F., Farrell, W. M., Slavin, J. A., Schatten, K. H., et al. (1995). The wind magnetic field investigation. *Space Science Reviews*, *71*, 207–229. https://doi.org/10.1007/BF00751330

Li, W., Ma, Q., Thorne, R. M., Bortnik, J., Zhang, X. J., Li, J., et al. (2016). Radiation belt electron acceleration during the 17 March 2015 geomagnetic storm: Observations and simulations. *Journal of Geophysical Research: Space Physics*, *121*(6), 5520–5536. https://doi.org/10.1002/2016JA022400

Li, W., Thorne, R. M., Bortnik, J., Baker, D. N., Reeves, G. D., Kanekal, S. G., et al. (2015). Solar wind conditions leading to efficient radiation belt electron acceleration: A superposed epoch analysis. *Geophysical Research Letters*, *42*(17), 6906–6915. https://doi.org/10.1002/2015GL065342

Li, W., Thorne, R. M., Ma, Q., Ni, B., Bortnik, J., Baker, D. N., et al. (2014). Radiation belt electron acceleration by chorus waves during the 17 March 2013 storm. *Journal of Geophysical Research: Space Physics*, *119*(6), 4681–4693. https://doi.org/10.1002/2014JA019945

Lugaz, N., Farrugia, C. J., Winslow, R. M., Al-Haddad, N., Kilpua, E. K. J., & Riley, P. (2016). Factors affecting the geoeffectiveness of shocks and sheaths at 1 AU. *Journal of Geophysical Research: Space Physics*, *121*(11), 10861–10879. https://doi.org/10.1002/2016JA023100

Malaspina, D. M., Ripoll, J.-F., Chu, X., Hospodarsky, G., & Wygant, J. (2018). Variation in plasmaspheric hiss wave power with plasma density. *Geophysical Research Letters*, *45*(18), 9417–9426. https://doi.org/10.1029/2018GL078564

Masías-Meza, J. J., Dasso, S., Démoulin, P., Rodriguez, L., & Janvier, M. (2016). Superposed epoch study of ICME sub-structures near Earth and their effects on Galactic cosmic rays. *Astronomy & Astrophysics*, *592*, A118. https://doi.org/10.1051/0004-6361/201628571

Mauk, B. H., Fox, N. J., Kanekal, S. G., Kessel, R. L., Sibeck, D. G., & Ukhorskiy, A. (2013). Science objectives and rationale for the radiation belt storm probes mission. *Space Science Reviews*, *179*(1–4), 3–27. https://doi.org/10.1007/s11214-012-9908-y

Miyoshi, Y., Kataoka, R., Kasahara, Y., Kumamoto, A., Nagai, T., & Thomsen, M. F. (2013). High-speed solar wind with southward interplanetary magnetic field causes relativistic electron flux enhancement of the outer radiation belt via enhanced condition of whistler waves. *Geophysical Research Letters*, *40*(17), 4520–4525. https://doi.org/10.1002/grl.50916

Moissard, C., Fontaine, D., & Savoini, P. (2019). A study of fluctuations in magnetic cloud-driven sheaths. *Journal of Geophysical Research: Space Physics*, *124*(11), 8208–8226. https://doi.org/10.1029/2019JA026952

Morley, S. K., Henderson, M. G., Reeves, G. D., Friedel, R. H. W., & Baker, D. N. (2013). Phase space density matching of relativistic electrons using the Van Allen Probes: REPT results. *Geophysical Research Letters*, *40*(18), 4798–4802. https://doi.org/10.1002/grl.50909

Moya, P. S., Pinto, V. A., Sibeck, D. G., Kanekal, S. G., & Baker, D. N. (2017). On the effect of geomagnetic storms on relativistic electrons in the outer radiation belt: Van Allen Probes observations. *Journal of Geophysical Research: Space Physics*, *122*(11), 11100–11108. https://doi.org/10.1002/2017JA024735

Murphy, K. R., Watt, C. E. J., Mann, I. R., Jonathan Rae, I., Sibeck, D. G., Boyd, A. J., et al. (2018). The global statistical response of the outer radiation belt during geomagnetic storms. *Geophysical Research Letters*, *45*(9), 3783–3792. https://doi.org/10.1002/2017GL076674

Nasi, A., Daglis, I. A., Katsavrias, C., & Li, W. (2020). Interplay of source/seed electrons and wave-particle interactions in producing relativistic electron PSD enhancements in the outer Van Allen belt. *Journal of Atmospheric and Solar-Terrestrial Physics*, *210*, 105405. https://doi.org/10.1016/j.jastp.2020.105405

O'Brien, T. P., McPherron, R. L., Sornette, D., Reeves, G. D., Friedel, R., & Singer, H. J. (2001). Which magnetic storms produce relativistic electrons at geosynchronous orbit? *Journal of Geophysical Research*, *106*(A8), 15533–15544. https://doi.org/10.1029/2001JA000052

Ogilvie, K. W., Chornay, D. J., Fritzenreiter, R. J., Hunsaker, F., Keller, J., Lobell, J., et al. (1995). SWE, a comprehensive plasma instrument for the wind spacecraft. *Space Science Reviews*, *71*, 55–77. https://doi.org/10.1007/BF00751326

Pinto, V. A., Bortnik, J., Moya, P. S., Lyons, L. R., Sibeck, D. G., Kanekal, S. G., et al. (2018). Characteristics, occurrence, and decay rates of remnant belts associated with three-belt events in the Earth's radiation belts. *Geophysical Research Letters*, *45*(22), 12099–12107. https://doi.org/10.1029/2018GL080274

Reeves, G. D., Friedel, R. H. W., Larsen, B. A., Skoug, R. M., Funsten, H. O., Claudepierre, S. G., et al. (2016). Energy-dependent dynamics of keV to MeV electrons in the inner zone, outer zone, and slot regions. *Journal of Geophysical Research: Space Physics*, *121*(1), 397–412. https://doi.org/10.1002/2015JA021569

Reeves, G. D., McAdams, K. L., Friedel, R. H. W., & O'Brien, T. P. (2003). Acceleration and loss of relativistic electrons during geomagnetic storms. *Geophysical Research Letters*, *30*(10), 1529. https://doi.org/10.1029/2002GL016513

Reeves, G. D., Spence, H. E., Henderson, M. G., Morley, S. K., Friedel, R. H. W., Funsten, H. O., et al. (2013). Electron acceleration in the heart of the Van Allen radiation belts. *Science*, *341*(6149), 991–994. https://doi.org/10.1126/science.1237743

Richardson, I. G., & Cane, H. V. (2010). Near-earth interplanetary coronal mass ejections during solar cycle 23 (1996–2009): Catalog and summary of properties. *Solar Physics*, *264*(1), 189–237. https://doi.org/10.1007/s11207-010-9568-6

Rodger, C. J., Carson, B. R., Cummer, S. A., Gamble, R. J., Clilverd, M. A., Green, J. C., et al. (2010). Contrasting the efficiency of radiation belt losses caused by ducted and nonducted whistler-mode waves from ground-based transmitters. *Journal of Geophysical Research: Space Physics*, *115*(A12), A12208. https://doi.org/10.1029/2010JA015880

Rodger, C. J., Kavanagh, A. J., Clilverd, M. A., & Marple, S. R. (2013). Comparison between POES energetic electron precipitation observations and riometer absorptions: Implications for determining true precipitation fluxes. *Journal of Geophysical Research: Space Physics*, *118*(12), 7810–7821. https://doi.org/10.1002/2013JA019439

Roederer, J. G. (1970). *Dynamics of geomagnetically trapped radiation*. Springer-Verlag. https://doi.org/10.1007/978-3-642-49300-3

Schiller, Q., Li, X., Blum, L., Tu, W., Turner, D. L., & Blake, J. B. (2014). A nonstorm time enhancement of relativistic electrons in the outer radiation belt. *Geophysical Research Letters*, *41*(1), 7–12. https://doi.org/10.1002/2013GL058485

Shprits, Y. Y., Kellerman, A., Aseev, N., Drozdov, A. Y., & Michaelis, I. (2017). Multi-MeV electron loss in the heart of the radiation belts. *Geophysical Research Letters*, *44*(3), 1204–1209. https://doi.org/10.1002/2016GL072258

Shprits, Y. Y., Thorne, R. M., Friedel, R., Reeves, G. D., Fennell, J., Baker, D. N., & Kanekal, S. G. (2006). Outward radial diffusion driven by losses at magnetopause. *Journal of Geophysical Research: Space Physics*, *111*(A11), A11214. https://doi.org/10.1029/2006JA011657

Shue, J. H., Song, P., Russell, C. T., Steinberg, J. T., Chao, J. K., Zastenker, G., et al. (1998). Magnetopause location under extreme solar wind conditions. *Journal of Geophysical Research*, *103*(A8), 17691–17700. https://doi.org/10.1029/98JA01103

Singer, H., Matheson, L., Grubb, R., Newman, A., & Bouwer, D. (1996). Monitoring space weather with the GOES magnetometers. In E. R. Washwell (Ed.), *GOES-8 and beyond* (Vol. 2812, pp. 299–308). International Society for Optical Engineering. https://doi.org/10.1117/12.254077

Spence, H. E., Reeves, G. D., Baker, D. N., Blake, J. B., Bolton, M., Bourdarie, S., et al. (2013). Science goals and overview of the radiation belt storm probes (RBSP) energetic particle, composition, and thermal plasma (ECT) suite on NASA's Van Allen Probes mission. *Space Science Reviews*, *179*, 311–336. https://doi.org/10.1007/s11214-013-0007-5

Su, Z., Zhu, H., Xiao, F., Zong, Q. G., Zhou, X. Z., Zheng, H., et al. (2015). Ultra-low-frequency wave-driven diffusion of radiation belt relativistic electrons. *Nature Communications*, *6*, 10096. https://doi.org/10.1038/ncomms10096

Summers, D., & Thorne, R. M. (2003). Relativistic electron pitch-angle scattering by electromagnetic ion cyclotron waves during geomagnetic storms. *Journal of Geophysical Research: Space Physics*, *108*(A4), 1143. https://doi.org/10.1029/2002JA009489

Thorne, R. M. (2010). Radiation belt dynamics: The importance of wave-particle interactions. *Geophysical Research Letters*, *37*(22), L22107. https://doi.org/10.1029/2010GL044990

Thorne, R. M., Li, W., Ni, B., Ma, Q., Bortnik, J., Chen, L., et al. (2013). Rapid local acceleration of relativistic radiation-belt electrons by magnetospheric chorus. *Nature*, *504*(7480), 411–414. https://doi.org/10.1038/nature12889

Tsyganenko, N. A., & Sitnov, M. I. (2005). Modeling the dynamics of the inner magnetosphere during strong geomagnetic storms. *Journal of Geophysical Research: Space Physics*, *110*(A3), A03208. https://doi.org/10.1029/2004JA010798

Turner, D. L., Angelopoulos, V., Li, W., Bortnik, J., Ni, B., Ma, Q., et al. (2014). Competing source and loss mechanisms due to wave-particle interactions in Earth's outer radiation belt during the 30 September to 3 October 2012 geomagnetic storm. *Journal of Geophysical Research: Space Physics*, *119*(3), 1960–1979. https://doi.org/10.1002/2014JA019770

Turner, D. L., Angelopoulos, V., Li, W., Hartinger, M. D., Usanova, M., Mann, I. R., et al. (2013). On the storm-time evolution of relativistic electron phase space density in Earth's outer radiation belt. *Journal of Geophysical Research: Space Physics*, *118*(5), 2196–2212. https://doi.org/10.1002/jgra.50151

Turner, D. L., Angelopoulos, V., Morley, S. K., Henderson, M. G., Reeves, G. D., Li, W., et al. (2014). On the cause and extent of outer radiation belt losses during the 30 September 2012 dropout event. *Journal of Geophysical Research: Space Physics*, *119*(3), 1530–1540. https://doi.org/10.1002/2013JA019446

Turner, D. L., Angelopoulos, V., Shprits, Y., Kellerman, A., Cruce, P., & Larson, D. (2012). Radial distributions of equatorial phase space density for outer radiation belt electrons. *Geophysical Research Letters*, *39*(9), L09101. https://doi.org/10.1029/2012GL051722

Turner, D. L., Kilpua, E. K. J., Hietala, H., Claudepierre, S. G., O'Brien, T. P., Fennell, J. F., et al. (2019). The response of Earth's electron radiation belts to geomagnetic storms: Statistics from the Van Allen Probes era including effects from different storm drivers. *Journal of Geophysical Research: Space Physics*, *124*, 1013–1034. https://doi.org/10.1029/2018JA026066

Turner, D. L., O'Brien, T. P., Fennell, J. F., Claudepierre, S. G., Blake, J. B., Jaynes, A. N., et al. (2017). Investigating the source of near-relativistic and relativistic electrons in Earth's inner radiation belt. *Journal of Geophysical Research: Space Physics*, *122*(1), 695–710. https://doi.org/10.1002/2016JA023600

Turner, D. L., O'Brien, T. P., Fennell, J. F., Claudepierre, S. G., Blake, J. B., Kilpua, E. K. J., & Hietala, H. (2015). The effects of geomagnetic storms on electrons in Earth's radiation belts. *Geophysical Research Letters*, *42*, 9176–9184. https://doi.org/10.1002/2015GL064747

Turner, D. L., Shprits, Y., Hartinger, M., & Angelopoulos, V. (2012). Explaining sudden losses of outer radiation belt electrons during geomagnetic storms. *Nature Physics*, *8*(3), 208–212. https://doi.org/10.1038/nphys2185

Turner, D. L., & Ukhorskiy, A. Y. (2020). Chapter 1 – Outer radiation belt losses by magnetopause incursions and outward radial transport: New insight and outstanding questions from the Van Allen Probes era. In A. N. Jaynes & M. E. Usanova (Eds.), *The dynamic loss of Earth's radiation belts* (pp. 1–28). Elsevier. Retrieved from http://www.sciencedirect.com/science/article/pii/B9780128133712000019

Usanova, M. E., Drozdov, A., Orlova, K., Mann, I. R., Shprits, Y., Robertson, M. T., et al. (2014). Effect of EMIC waves on relativistic and ultrarelativistic electron populations: Ground-based and Van Allen Probes observations. *Geophysical Research Letters*, *41*(5), 1375–1381. https://doi.org/10.1002/2013GL059024

Yermolaev, Y. I., Lodkina, I. G., Nikolaeva, N. S., & Yermolaev, M. Y. (2015). Dynamics of large-scale solar wind streams obtained by the double superposed epoch analysis. *Journal of Geophysical Research: Space Physics*, *120*(9), 7094–7106. https://doi.org/10.1002/2015JA021274

Yermolaev, Y. I., Lodkina, I. G., Nikolaeva, N. S., & Yermolaev, M. Y. (2017). Dynamics of large-scale solar-wind streams obtained by the double superposed epoch analysis: 2. Comparisons of CIRs vs. Sheaths and MCs vs. Ejecta. *Solar Physics*, *292*(12), 193. https://doi.org/10.1007/s11207-017-1205-1

Yermolaev, Y. I., Lodkina, I. G., Nikolaeva, N. S., Yermolaev, M. Y., Riazantseva, M. O., & Rakhmanova, L. S. (2018). Statistic study of the geoeffectiveness of compression regions CIRs and Sheaths. *Journal of Atmospheric and Solar-Terrestrial Physics*, *180*, 52–59. https://doi.org/10.1016/j.jastp.2018.01.027

Zhang, X. J., Li, W., Thorne, R. M., Angelopoulos, V., Ma, Q., Li, J., et al. (2016). Physical mechanism causing rapid changes in ultrarelativistic electron pitch angle distributions right after a shock arrival: Evaluation of an electron dropout event. *Journal of Geophysical Research: Space Physics*, *121*(9), 8300–8316. https://doi.org/10.1002/2016JA022517

Zhao, H., Baker, D. N., Li, X., Malaspina, D. M., Jaynes, A. N., & Kanekal, S. G. (2019). On the acceleration mechanism of ultrarelativistic electrons in the center of the outer radiation belt: A statistical study. *Journal of Geophysical Research: Space Physics*, *124*(11), 8590–8599. https://doi.org/10.1029/2019JA027111